Nonlinear interactions in strained axisymmetric high-Reynolds-number turbulence

By S. AYYALASOMAYAJULA AND Z. WARHAFT

Sibley School of Mechanical and Aerospace Engineering, Cornell University, Ithaca, NY 14853, USA

We present measurements, over a wide range of Reynolds numbers ($40 \leqslant R_\lambda \leqslant 470$), of grid-generated turbulence subjected to axisymmetric strain, and of the subsequent evolution of the turbulence after the strain is released. The Reynolds number was varied by the use of both passive and active grids and the strain was produced by a 4:1 area-change axisymmetric contraction placed at various distances from the grid. The time scale ratio of the turbulence to that of the mean strain varied from approximately 10 to 30. The results show reasonable agreement with (linear) rapid distortion theory (RDT) for the velocity variances but, contrary to linear theory, the strained longitudinal, u_1, spectrum peaked at significantly higher wavenumber than the transverse, u_2, spectrum. The mismatch in peaks increased with increasing R_λ and at the highest Reynolds number ($R_\lambda = 470$) the peak of the strained u_1-spectrum occurred at a wavenumber 200 times greater than that of the u_2-spectrum. As the flow relaxed toward isotropy after the contraction, further evidence of the non-locality in the flow field became apparent, with a second peak in the u_2-spectrum emerging at a similar wavenumber to the high-frequency peak in the u_1-spectrum. The strain also caused the longitudinal derivative skewness to change sign but as the flow evolved after the contraction the derivative skewness returned to its typical value of -0.4. We also show that single-point turbulence models are inadequate to describe the relaxation of the turbulence towards an isotropic state in the postcontraction region.

1. Introduction

The way in which the mean strain affects the structure of turbulence is of importance in understanding environmental flows such as flow over water and hills (Hunt & Snyder 1980; Belcher & Hunt 1998), the flow in machinery and in wind-tunnel contractions (Goldstein 1951; Batchelor 1953; Townsend 1954; Goldstein & Durbin 1980), and the flow over and around obstacles (Hunt 1973; Hunt & Carruthers 1990; Hunt *et al.* 1990). The subject is also of fundamental interest since it highlights the interaction of various turbulence scales. Straining generally distorts the large eddies more strongly than the small ones (Kida & Hunt 1989; Tsinober 2001) and understanding the ensuing scale–scale interactions is central to understanding the turbulence dynamics itself.

Early on (Prandtl 1933; Taylor 1933; Batchelor 1953) it was realized that if the mean strain is applied rapidly, inertia and viscous forces arising from the turbulence may be neglected and the problem becomes linear. For this condition it may be assumed that each spectral mode is acted on equally by the suddenly applied strain and that they evolve independently (see below). For reviews of the linear theory, known as rapid-distortion theory (RDT) see Savill (1987) and Hunt & Carruthers

(1990). The requirements of RDT are stringent, and in any real flow the turbulence time scale is comparable with that of the strain. Under these conditions nonlinear effects may become significant. Surprisingly there has been very little experimental work done on this problem at high Reynolds numbers, where the effects of the strain are prevalent over a large wavenumber range but do not act uniformly on the various scales. Because the eddy time scale decreases with decreasing scale size, the smaller eddies respond 'less rapidly' than the large ones. Under these conditions we may expect complex interplay between the different scales.

Here we address perhaps the most classical of the turbulence strain experiments, the flow of turbulence through an axisymmetric contraction (Batchelor 1953; Batchelor & Proudman 1954). For this flow there have been number of experimental studies (Uberoi 1956; Pearson 1959; Mills & Corrsin 1959; Tucker & Reynolds 1968; Reynolds & Tucker 1975; Warhaft 1980; Sjogren & Johansson 1998; Choi & Lumley 2001) and some direct numerical simulations (Lee 1985; Lee & Reynolds 1985). Earlier, Ribner & Tucker (1953) had calculated the effects of axisymmetric contraction on turbulence using RDT with an idealized spectrum. With the exception of the recent work of Sjogren & Johansson (1998), the Reynolds number of the turbulence subjected to the strain has been low, generally in the Taylor Reynolds number (R_λ, defined below) range of 50 or less. For these low Reynolds numbers the spectrum falls off rapidly and the flow is dominated by the energy-containing eddies. There is little opportunity for spectral interaction over an appreciable wavenumber range, and it is therefore not possible to examine nonlinear effects between various scales. In particular long-range interactions are precluded. It is the objective of the present work to address this issue by subjecting nearly isotropic turbulence over a broad Reynolds-number range ($40 \leqslant R_\lambda \leqslant 470$) to axisymmetric contraction. By systematically increasing the Reynolds number we will show that the distorted flow departs more and more from linear theory and at the highest Reynolds numbers there is a rich and complex interaction of the various scales.

Apart from the problem of how the turbulence is affected by the mean strain, there is another question that deserves attention in its own right: for an anisotropic turbulence field, how does the flow relax back towards the isotropic state? In particular, information on the speed at which it occurs and the route it takes is required. There has been much work on this problem too (Rotta 1951; Launder, Reece & Rodi 1975; Lumley & Newman 1977; Gence & Mathieu 1980; Newman, Launder & Lumley 1981; Reynolds & Kassinos 1995; Chung & Kim 1995; Kassinos, Reynolds & Rogers 2001). Here the emphasis has been on developing models, and these have relied again on data from the low-Reynolds-number experiments cited above. In the present work we will also examine the return to isotropy of the turbulence distorted by an axisymmetric contraction. Because, as we will show, the turbulence field produced at the exit of the contraction is complex, we might expect that the return to isotropy will not comply with simple theory or single-point modelling. We will show this to be the case.

2. Flow parameters and governing equations

2.1. *Flow parameters*

The parameters which govern the behaviour of the strained turbulence are the Taylor-scale Reynolds number ($R_\lambda \equiv \langle u_1^2 \rangle^{1/2} \lambda / \nu$, where u_1 is the longitudinal fluctuating velocity component and the angle brackets denote time averaging, λ is the Taylor microscale $[\langle U_1 \rangle^2 \langle u_1^2 \rangle / \langle (\partial u_1 / \partial t)^2 \rangle]^{1/2}$ with $\langle U_1 \rangle$ the mean velocity and ν the kinematic
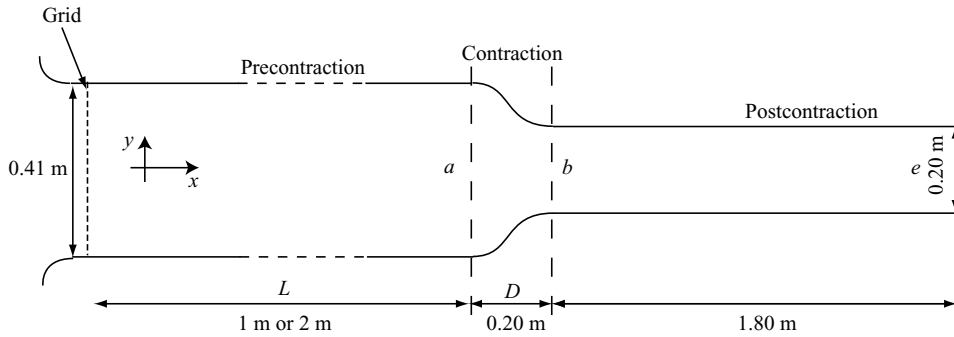
FIGURE 1. Schematic of experimental setup. Two different precontraction sections were used (see text). Active and passive grids were used to vary the Reynolds numbers. a and b are the immediate pre- and postcontraction regions respectively. e is the furthest downstream distance location, 153 cm from the end of the contraction.

viscosity), the initial anisotropy and the time-scale ratio of the imposed strain rate and that of the turbulence (to be defined below).

The total strain in the longitudinal direction, c, is defined as (Lee 1989; Pope 2000)

$$c \equiv \exp\left[\int_a^b \frac{\partial \langle U_1 \rangle}{\partial x_1}\, \mathrm{d}t\right] \tag{2.1}$$

where a and b denote measurement stations before and after the contraction (figure 1).

Owing to the symmetry, $\partial \langle U_1 \rangle/\partial x_2 = \partial \langle U_1 \rangle/\partial x_3 = 0$ and hence $\mathrm{d}\langle U_1 \rangle/\mathrm{d}x_1 = \partial \langle U_1 \rangle/\partial x_1$. Also, $\mathrm{d}t = \mathrm{d}x_1/\langle U_1 \rangle$. Substituting these simplifications into (2.1) gives

$$c = \frac{\langle U_{1_b} \rangle}{\langle U_{1_a} \rangle}. \tag{2.2}$$

Similarly it can be shown that the total strain in the x_2 and the x_3 directions is $1/\sqrt{c}$ for the axisymmetric case.

We define a non-dimensional time-scale ratio

$$S^* \equiv 2Sk/\langle \varepsilon \rangle. \tag{2.3}$$

Here k is the turbulent kinetic energy $\frac{1}{2}(\langle u_1^2 \rangle + 2\langle u_2^2 \rangle)$ where u_2 is the transverse velocity fluctuation and the flow is axisymmetric (so that $u_2 = u_3$, u_3 being the transverse component orthogonal to u_2), $\langle \varepsilon \rangle$ is the mean turbulence dissipation rate, determined before the contraction by the expression $15(\nu/\langle U_1 \rangle^2)\langle(\partial u_1/\partial t)^2\rangle$, and S is the strain rate, defined by

$$S \equiv \sqrt{S_{ij}S_{ij}/2} \tag{2.4}$$

where the S_{ij} are the components of the second-order strain-rate tensor (Lee & Reynolds 1985).

Clearly the quantity S is not constant through the contraction but changes owing to energy decay as well as the varying strain. In order to parameterize the effect of the contraction we define a strain rate $\bar{S}$ as

$$\bar{S} = \frac{\sqrt{3}}{2} \frac{\langle U_{1_a} \rangle}{D}\left(\frac{\langle U_{1_b} \rangle}{\langle U_{1_a} \rangle} - 1\right) \tag{2.5}$$

where D is the length of the contraction. This is obtained using (2.4) and by linearizing the strain rate for our geometry. It uniquely determines the relative rapidness of the distortion of our flow. Further, we define a non-dimensional mean strain $\overline{S}^*$ by substituting (2.5) into (2.3). With $k/\langle\varepsilon\rangle$ measured at station a, we will use $\overline{S}^*$ to compare the various flows studied here.

2.2. Equations governing the distortion

For incompressible homogeneous turbulent flows, the velocity fluctuations evolve as

$$\frac{\mathrm{D}u_j}{\mathrm{D}t} = -u_i\frac{\partial\langle U_j\rangle}{\partial x_i} - u_i\frac{\partial u_j}{\partial x_i} + \nu\nabla^2 u_j - \frac{1}{\rho}\frac{\partial p'}{\partial x_j} \tag{2.6}$$

where the operator $\mathrm{D}/\mathrm{D}t$ is the material derivative following the mean flow.

The Poisson equation for the fluctuating pressure $p' = p^{(r)} + p^{(s)} + p^{(h)}$ (where $p^{(r)}$ is the rapid-pressure component, related to the mean velocity gradients, $p^{(s)}$ is the slow-pressure component, related to the fluctuating velocity gradient, and $p^{(h)}$ is the homogeneous pressure component, which is a solution to Laplace equation and satisfies the boundary conditions for pressure; see Pope 2000) may be written as

$$\frac{1}{\rho}\nabla^2(p^{(r)} + p^{(s)} + p^{(h)}) = -2\frac{\partial\langle U_i\rangle}{\partial x_j}\frac{\partial u_j}{\partial x_i} - \frac{\partial^2 u_i u_j}{\partial x_i\partial x_j}. \tag{2.7}$$

The equation for the fluctuating vorticity with irrotational mean flow is

$$\frac{\mathrm{D}\omega_j}{\mathrm{D}t} = \omega_i\frac{\partial\langle U_j\rangle}{\partial x_i} + \nu\nabla^2\omega_j - \left[u_k\frac{\partial\omega_j}{\partial x_k} - \left\langle u_k\frac{\partial\omega_j}{\partial x_k}\right\rangle\right] + \left[\omega_k\frac{\partial u_j}{\partial x_k} - \left\langle\omega_k\frac{\partial u_j}{\partial x_k}\right\rangle\right]. \tag{2.8}$$

Under the rapid-distortion theory (RDT) assumption, where the turbulent inertial and viscous terms are neglected, the above equations simplify to

$$\frac{\mathrm{D}u_j}{\mathrm{D}t} = -u_i\frac{\partial\langle U_j\rangle}{\partial x_i} - \frac{1}{\rho}\frac{\partial p^{(r)}}{\partial x_j}, \tag{2.9}$$

$$\frac{1}{\rho}\nabla^2 p^{(r)} = -2\frac{\partial\langle U_i\rangle}{\partial x_j}\frac{\partial u_j}{\partial x_i}, \tag{2.10}$$

$$\frac{\mathrm{D}\omega_j}{\mathrm{D}t} = \omega_i\frac{\partial\langle U_j\rangle}{\partial x_i}. \tag{2.11}$$

For this case it can be shown that the final state after the distortion depends only on the total amount of strain and the geometry of the strain. Here, the Fourier modes evolve independently (for detailed proofs see Ribner & Tucker 1953; Pope 2000). Hence, the energy-spectrum tensor components after the distortion can be obtained explicitly as a function of the total distortion (which is axisymmetric and irrotational and is uniquely identified by c) and the initial spectrum (Batchelor 1953; Ribner & Tucker 1953; Lee 1986; Lee & Reynolds 1985; Lee 1989). From the energy-spectrum tensor components one can obtain the Reynolds stresses and the energy and dissipation spectra. For our flow $c = 4$, and RDT yields $\langle u_{2_b}^2\rangle^{1/2}/\langle u_{2_a}^2\rangle^{1/2} = 0.45$, $\langle u_{1_b}^2\rangle^{1/2}/\langle u_{1_a}^2\rangle^{1/2} = 1.75$ and $k_b/k_a = 1.27$.

For the rapid-distortion assumption to hold strictly for a given flow, the flow must satisfy the condition $S\tau_\eta \gg 1$, where τ_η ($\equiv (\langle\varepsilon\rangle/\nu)^{1/2}$ with ν the kinematic viscosity) is the Kolmogorov time scale. This condition implies that the distortion is rapid even when compared with the smallest scales (which are the most rapid scales present in the turbulent flow field). A weaker condition is $S^* \gg 1$. Even this second condition is apparently difficult to meet. For the flow presented here $S^* \sim 10$, and to have a flow

for which $S^* \sim 10^4$, say, the contraction would have to be so short (a few millimetres), that there would be secondary flows or other adverse effects. Thus we must see the distortion as acting in a modulated way on the various scales of a flow when R_λ is sufficiently high that there is a broad spectrum.

Returning to the full equation for u_j (2.6), we may obtain a transport equation for the velocity variances $\langle u_i u_j \rangle$,

$$\frac{D\langle u_i u_j \rangle}{Dt} = P_{ij} + R_{ij} - \varepsilon_{ij} - \frac{\partial}{\partial x_k} T_{kij} \tag{2.12}$$

where P_{ij} is the production term, R_{ij} is the redistribution term, ε_{ij} is the viscous-dissipation term and T_{kij} is the Reynolds stress-flux term. These terms are defined in the following way:

$$P_{ij} = -\langle u_i u_k \rangle \frac{\partial \langle U_j \rangle}{\partial x_k} + \langle u_j u_k \rangle \frac{\partial \langle U_i \rangle}{\partial x_k}, \tag{2.13}$$

$$R_{ij} = \left\langle \frac{p'}{\rho} \left(\frac{\partial u_i}{\partial x_j} + \frac{\partial u_j}{\partial x_i} \right) \right\rangle, \tag{2.14}$$

$$\varepsilon_{ij} = 2\nu \left\langle \frac{\partial u_i}{\partial x_k} \frac{\partial u_j}{\partial x_k} \right\rangle, \tag{2.15}$$

$$T_{kij} = T_{kij}^{(u)} + T_{kij}^{(p)} + T_{kij}^{(v)}, \tag{2.16}$$

where $T_{kij}^{(u)} \equiv \langle u_i u_j u_k \rangle$, $T_{kij}^{(p)} \equiv \rho^{-1} \langle u_i p' \rangle \delta_{jk} + \rho^{-1} \langle u_j p' \rangle \delta_{ik}$ and $T_{kij}^{(v)} \equiv -\nu \partial \langle u_i u_j \rangle / \partial x_k$.

Further, the following incompressible relationships for the flow through the contraction can be used to simplify the above relations:

$$\frac{\partial \langle U_1 \rangle}{\partial x_1} = -\frac{1}{2} \frac{\partial \langle U_2 \rangle}{\partial x_2} = -\frac{1}{2} \frac{\partial \langle U_3 \rangle}{\partial x_3}, \tag{2.17}$$

$$\frac{\partial \langle U_i \rangle}{\partial x_j} = 0 \quad \text{for} \quad j \neq i. \tag{2.18}$$

The whole flow field is homogenous in the transverse directions before and after the contraction and in the contraction. Owing to this symmetry, $\langle u_i u_j \rangle = 0$ for $i \neq j$ and $\langle u_2^2 \rangle = \langle u_3^2 \rangle$.

Using (2.17) and (2.18) and the symmetry conditions, the variance transport equations in the contraction become

$$\frac{D}{Dt} \langle u_1^2 \rangle = -2\langle u_1^2 \rangle \frac{\partial \langle U_1 \rangle}{\partial x_1} - 2\nu \left\langle \frac{\partial u_1}{\partial x_k} \frac{\partial u_1}{\partial x_k} \right\rangle - \frac{2}{\rho} \left\langle u_1 \frac{\partial p'}{\partial x_1} \right\rangle - \frac{\partial}{\partial x_k} \langle u_1^2 u_k \rangle + \nu \frac{\partial^2 \langle u_1^2 \rangle}{\partial x_k \partial x_k}, \tag{2.19}$$

$$\frac{D}{Dt} \langle u_2^2 \rangle = \langle u_2^2 \rangle \frac{\partial \langle U_1 \rangle}{\partial x_1} - 2\nu \left\langle \frac{\partial u_2}{\partial x_k} \frac{\partial u_2}{\partial x_k} \right\rangle - \frac{2}{\rho} \left\langle u_2 \frac{\partial p'}{\partial x_2} \right\rangle - \frac{\partial}{\partial x_k} \langle u_2^2 u_k \rangle + \nu \frac{\partial^2 \langle u_2^2 \rangle}{\partial x_k \partial x_k}. \tag{2.20}$$

The equation for $\langle u_3^2 \rangle$ is identical to (2.20) but with the index 2 replaced by 3. The dominant effect on the variances is due to the mean strain. In the axisymmetric contraction the mean strain rate in the x_1 direction ($\partial \langle U_1 \rangle / \partial x_1$) is positive and hence, owing to the net negative sign of the first term on the right-hand side of (2.19), the variance $\langle u_1^2 \rangle$ decreases with evolution time. Similarly, owing to the net positive sign of the mean strain term in (2.20) and in the corresponding equation for $\langle u_3^2 \rangle$, these variances increase with evolution time.

The turbulent kinetic energy equation (half the sum of the $\langle u_1^2 \rangle$ and $\langle u_2^2 \rangle$ equations and the corresponding $\langle u_3^2 \rangle$ equation) is

$$\frac{\mathrm{D}k}{\mathrm{D}t} = [\langle u_2^2 \rangle - \langle u_1^2 \rangle]\frac{\partial \langle U_1 \rangle}{\partial x_1} - \nu \left\langle \frac{\partial u_i}{\partial x_k}\frac{\partial u_i}{\partial x_k} \right\rangle - \frac{1}{2}\frac{\partial}{\partial x_k}\langle u_i u_i u_k \rangle - \frac{1}{\rho}\left\langle u_i \frac{\partial p'}{\partial x_i} \right\rangle + \frac{\nu}{2}\frac{\partial^2 \langle u_i u_i \rangle}{\partial x_k \partial x_k}. \tag{2.21}$$

The first term on the right-hand side of (2.21), which is the leading term, and gives the effect of the mean strain on the turbulent kinetic energy, is positive indicating an increase in net kinetic energy owing to the effect of the contraction.

Below we will be comparing our measurements with linear theory (RDT). We are aware that RDT calls for strict homogeneity in the applied strain (Lee 1989; Pope 2000). Here we use it as a framework in which to report our measurements. In order to determine the strained spectra we use a procedure similar to that of Ribner & Tucker (1953) (see also Lee & Reynolds 1985; Lee 1989). We model the initial energy-spectrum function $E(\kappa)$ in accordance with Pope (2000) as

$$E(\kappa) = C\langle \varepsilon \rangle^{2/3} \kappa^{-5/3} f_\ell(\kappa\ell) f_\eta(\kappa\eta) \tag{2.22}$$

where

$$f_\ell(\kappa\ell) = \left(\frac{\kappa\ell}{[(\kappa\ell)^2 + c_\ell]^{1/2}}\right)^{11/3}, \quad f_\eta(\kappa\eta) = \exp\left(-\beta\left\{[(\kappa\eta)^4 + c_\eta^4]^{1/4} - c_\eta\right\}\right) \tag{2.23}$$

and κ is the magnitude of the wavenumber vector $\boldsymbol{\kappa} \equiv \kappa_i\hat{\boldsymbol{e}}_i$. The Kolmogorov constant C is taken to be 1.5 and the model constant β is taken to be 5.2 (Pope 2000). The two model constants c_ℓ and c_η are determined from the experimental data, as are ℓ (the integral length scale) and η (the Kolmogorov length scale).

By definition, for an isotropic turbulence field the energy-spectrum function and energy-spectrum tensor components are related by

$$\Phi_{ij}(\boldsymbol{\kappa}) = \frac{E(\kappa)}{4\pi\kappa^2}\left(\delta_{ij} - \frac{\kappa_i\kappa_j}{\kappa^2}\right). \tag{2.24}$$

The one-dimensional energy spectrum, which can be measured using hot-wire anemometry and Taylor's hypothesis, is related to the energy-spectrum tensor components by

$$E_{ij}(\kappa_1) = 2\int\int_{-\infty}^{\infty}\Phi_{ij}(\boldsymbol{\kappa})\,\mathrm{d}\kappa_2\,\mathrm{d}\kappa_3. \tag{2.25}$$

The distorted energy-spectrum tensor components (starred quantities, below) for an axisymmetric contraction can be derived from the expressions given in Lee (1989) (see also Lee 1986; Lee & Reynolds 1985; Lee, Piomelli & Reynolds 1986) and the use of (2.1), (2.2), (2.17) and (2.18):

$$\Phi_{11}^*(\boldsymbol{\kappa}^*) = \frac{E(\kappa)}{4\pi c^2}\frac{\kappa_2^2 + \kappa_3^2}{\left(c^{-3}\kappa_1^2 + \kappa_2^2 + \kappa_3^2\right)^2}, \tag{2.26}$$

$$\Phi_{22}^*(\boldsymbol{\kappa}^*) = \frac{E(\kappa)}{4\pi}\frac{c}{\left(c^{-3}\kappa_1^2 + \kappa_2^2 + \kappa_3^2\right)^2}\left[c^{-3}\kappa_1^2 + \kappa_3^2 - \frac{(1 - c^{-3})\kappa_1^2\kappa_3^2}{\kappa_1^2 + \kappa_2^2 + \kappa_3^2}\right], \tag{2.27}$$

where the distorted wavenumber vector $\boldsymbol{\kappa}^*$ is related to the wavenumber vector $\boldsymbol{\kappa}$ in the following way:

$$\boldsymbol{\kappa}^* = \frac{\kappa_1}{c}\hat{\boldsymbol{e}}_1 + c^{1/2}\kappa_2\hat{\boldsymbol{e}}_2 + c^{1/2}\kappa_3\hat{\boldsymbol{e}}_3. \tag{2.28}$$

To calculate the distorted one-dimensional spectra the following relationship is used:

$$E_{ij}^*(\kappa_1) = \frac{2}{c} \int \int_{-\infty}^{\infty} \Phi_{ij}^*(\boldsymbol{\kappa}^*) \, d\kappa_2^* \, d\kappa_3^* \qquad (2.29)$$

where κ_1 is the wavenumber in the precontraction section.

In the work below whenever we compare the precontraction and postcontraction spectra, the distorted one-dimensional energy spectra have been normalized in such a way that they share the same wavenumber space as the original one-dimensional energy spectra. Hence when the one-dimensional spectra are obtained experimentally the local wavenumber space needs to be stretched out by a factor c and, correspondingly, the spectra by a factor $1/c$.

The model has two unknown constants, c_ℓ and c_η, and they are determined from measurements of the kinetic energy, the dissipation rate, the integral length scale and the Kolmogorov length scale. These flow quantities are calculated using only the measurements of the longitudinal velocity fluctuations u_1 at measurement station a (figure 1). The model constants are then used to obtain an initial three-dimensional velocity-spectrum function. Using the RDT relationships between the spectrum functions and the isotropic-model spectrum function obtained above, the distorted three-dimensional spectrum function is then computed. This is used to obtain the u_1 one-dimensional distorted spectrum, $E_{11}^*(\kappa_1)$. A similar procedure, based only on transverse fluctuation (u_2) measurements as input to the model spectrum, is followed to obtain the u_2 one-dimensional distorted-spectrum function, $E_{22}^*(\kappa_1)$, using the isotropic flow quantities. We have verified that this method, in which the u_1 and u_2 distorted spectra are independently estimated from their respective precontraction parameters, gives qualitatively similar results to a true isotropic calculation.

Using (2.22), (2.26), (2.27) and (2.29) and the following relationships between the longitudinal derivatives of the velocity fluctuations and the one-dimensional spectra,

$$\left\langle \left(\frac{\partial u_1}{\partial x_1} \right)^2 \right\rangle = \int_0^\infty \kappa_1^2 E_{11}^*(\kappa_1) \, d\kappa_1, \qquad (2.30)$$

$$\left\langle \left(\frac{\partial u_2}{\partial x_1} \right)^2 \right\rangle = \int_0^\infty \kappa_1^2 E_{22}^*(\kappa_1) \, d\kappa_1, \qquad (2.31)$$

the small-scale anisotropy ratio, $(\partial u_2/\partial x_1)^2/(\partial u_1/\partial x_1)^2$ (which has the value 2 for isotropic turbulence), can be calculated for this axisymmetric distortion to be around 7. (This value is slightly dependent on the form of the model spectrum in the dissipation range.)

2.3. *The equations governing the return to isotropy*

For the postcontraction region between stations b and e (figure 1) the flow is decaying-homogeneous anisotropic turbulence. The variance of the turbulent velocity fluctuations evolves according to

$$\frac{d}{dt} \langle u_i u_j \rangle = \mathscr{R}_{ij}^{(s)} - \varepsilon_{ij}, \qquad (2.32)$$

$$\mathscr{R}_{ij}^{(s)} \equiv \left\langle \frac{p^{(s)}}{\rho} \left(\frac{\partial u_i}{\partial x_j} + \frac{\partial u_j}{\partial x_i} \right) \right\rangle, \qquad (2.33)$$

$$\varepsilon_{ij} \equiv 2v \left\langle \frac{\partial u_i}{\partial x_k} \frac{\partial u_i}{\partial x_k} \right\rangle, \qquad (2.34)$$

$$\frac{1}{\rho}\nabla^2 p^{(s)} = -2\frac{\partial^2}{\partial x_i \partial x_j}(u_i u_j - \langle u_i u_j \rangle),\tag{2.35}$$

where $\mathscr{R}_{ij}^{(s)}$ is the slow-pressure rate-of-strain tensor (Pope 2000). For high-Reynolds-number flows where the small scales are locally isotropic (we will show below that after the contraction the small scales quickly become isotropic), the dissipation term ε_{ij} can be approximated as

$$\varepsilon_{ij} = \frac{2}{3}\langle \varepsilon \rangle \delta_{ij}.\tag{2.36}$$

For the study of the return to isotropy (Pope 2000) it is convenient look at the normalized anisotropy tensor b_{ij}, defined as

$$b_{ij} \equiv \frac{\langle u_i u_j \rangle}{2k} - \frac{1}{3}\delta_{ij}.\tag{2.37}$$

Hence, (2.32) can be rewritten using (2.36) and (2.37) as

$$\frac{\mathrm{d}}{\mathrm{d}t}b_{ij} = \frac{\langle \epsilon \rangle}{k}\left(b_{ij} + \frac{\mathscr{R}_{ij}^{(s)}}{2\langle \varepsilon \rangle}\right).\tag{2.38}$$

The linear model for $\mathscr{R}_{ij}^{(s)}$ proposed by Rotta (1951) is

$$\mathscr{R}_{ij}^{(s)} = -2C_R\langle \varepsilon \rangle b_{ij}\tag{2.39}$$

where C_R is Rotta's constant.

By introducing a non-dimensional time coordinate s ($\mathrm{d}s \equiv \langle \varepsilon \rangle/k\mathrm{d}t$), (2.38) simplifies to

$$\frac{\mathrm{d}}{\mathrm{d}s}b_{ij} = -(C_R - 1)b_{ij}.\tag{2.40}$$

From (2.40) it follows that the normalized anisotropy ratios b_{ij} follow an exponential path to isotropy. We will show that this model is inadequate, since C_R is not constant but varies with the initial conditions. Even for a specific flow C_R is found to vary as the flow evolves. A more general model would involve a nonlinear return to isotropy, i.e. the return to isotropy would depend on quantities like $b_{ik}b_{kj}$, $b_{ik}b_{kl}b_{lj}$ etc. We will show below that models which rely on a single-point description of the state of turbulence are inadequate to describe our high-Reynolds-number experiments. Our results suggest that any model which does not take into account the complete spectral state of the turbulence will also be inadequate.

3. Apparatus

Measurements were performed in the low-background-turbulence open-circuit square-section (40.7×40.7 cm^2) wind tunnel (figure 1) described in Sirivat & Warhaft (1983) (see also Warhaft 1980). Various passive and active grids were used to generate turbulence over a large Reynolds-number range. The mesh lengths for the passive grids were 2.54 cm and 5.08 cm. The active grid had a mesh length of 5.08 cm and was operated in both synchronous and random modes (Mydlarski & Warhaft 1996). First described by Makita (1991), the grid has triangular agitator wings on each grid mesh. The bars are rotated and the direction of rotation is randomly switched, resulting in a flapping motion. The motion of these wings enhances both the integral scale and the turbulence intensity. The Reynolds number was varied from 100 to 470
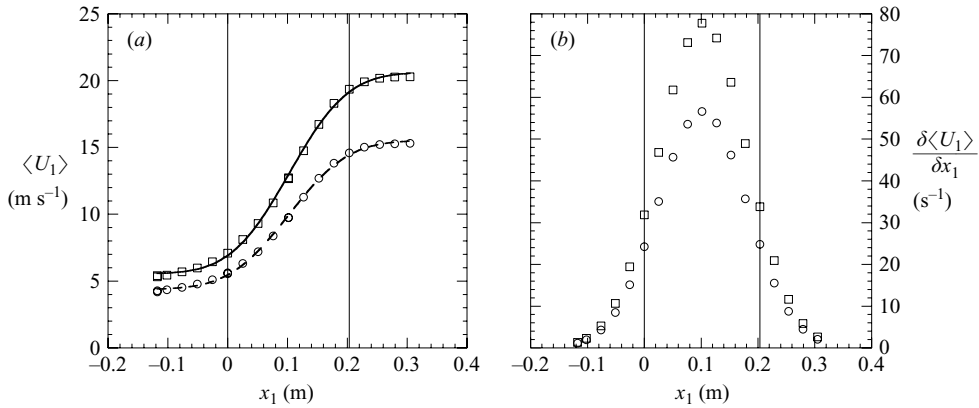
FIGURE 2. (*a*) The variation of mean velocity in the contraction for two typical cases. (*b*) The variation of strain rate in the contraction. Squares, $R_\lambda = 44$, 2.54-cm-mesh passive grid, short precontraction; circles, $R_\lambda = 260$, 5.08-cm-mesh active grid random mode, long precontraction. The solid line are scaled error function fits to the data. The vertical lines are the locations of the contraction. The abscissa is the downstream distance measured from the contraction.

with the active grid and from 40 to 100 with the passive grids. For both grid types the variation was caused by changing the mean wind speed.

Hot-wire anemometry was employed to measure the velocity fluctuations. Simultaneous u_1 and u_2 fluctuations were measured using an X-wire array. The wires were 3.05 μm in diameter and made of tungsten. The length-to-diameter ratio was about 200. The probes were connected to Dantec 55M01 constant-temperature bridges and were operated at an overheat ratio of 1.8. The signals were high-pass filtered (typically less than 0.01 Hz) to eliminate low-frequency noise and low-pass filtered to eliminate high-frequency noise. The data was digitized using a 12 bit A/D converter, and typically 10^7 samples were taken. Further details of the experimental procedure can be found in Mydlarski & Warhaft (1996, 1998).

An axisymmetric contraction of fixed 4:1 area ratio was used to produce the axisymmetric distortion (Warhaft 1980). The contraction was 20.3 cm long and was placed at two distances, nominally 100 cm and 200 cm from the grid (the exact distances vary slightly with the grid used; see the table 1 caption). These setups are referred to from here on as the short precontraction and the long precontraction. The contraction profile was a seventh-order polynomial, which can be uniquely determined using the constraints of zero slope, curvature and third derivatives at the end points and the halving of the width along the length of the contraction (see Warhaft 1980). Figure 2(*a*) shows the mean velocity profiles for a 2.54 cm mesh-length passive grid with the short precontraction ($R_\lambda = 44$) and for the active grid in the random mode with the long precontraction ($R_\lambda = 260$). The fits are scaled error functions. Note the variation in mean velocity in the post- and precontraction region. Figure 2(*b*) shows the derivative of the mean profile, $\partial\langle U_1\rangle/\partial x_1$, i.e. the variation of the strain rate in the contraction.

Earlier in the course of measurements the presence of an acoustic mode was detected in all the precontraction data for the short precontraction lengths. This acoustic mode was dominant at the low-wavenumber region of the spectrum in all the active-grid runs, but was weaker in the passive-grid experiments. In order to

(a)

| | Passive, $M = 2.54$ cm | | Passive, $M = 5.08$ cm | | | |
| | Short precontraction | | Short precontraction | | Long precontraction | |
	Min R_λ	Max R_λ	Min R_λ	Max R_λ	Min R_λ	Max R_λ
R_{λ_a}	38.2	43.8	47.3	72	34.9	52.1
x_a/M	29.5	29.5	14.8	14.8	38.8	38.8
$\langle U_{1_a}\rangle$(m s^{-1})	3.43	5.18	2.40	4.81	2.47	4.80
$\langle u_{1_a}^2\rangle^{1/2}/\langle U_{1_a}\rangle$(%)	3.36	3.32	5.94	6.19	2.53	2.70
$\langle u_{1_a}^2\rangle^{1/2}/\langle u_{2_a}^2\rangle^{1/2}$	1.14	1.05	1.06	1.00	1.00	0.97
ℓ_a(cm)	1.26	1.11	1.57	1.74	1.95	2.09
λ_a(mm)	4.97	3.82	4.98	3.62	8.38	6.02
η_a(mm)	0.408	0.293	0.368	0.217	0.720	0.424
$\langle\epsilon_a\rangle$(m^2/sec^3)	0.121	0.459	0.183	1.53	0.0125	0.104
$\dfrac{\langle(\partial u_2/\partial x)^2\rangle}{\langle(\partial u_1/\partial x)^2\rangle}$	1.74	1.85	1.70	1.95	1.73	1.87

(b)

| | Active, synchronous mode | | Active, random mode | | | |
| | Short precontraction | | Short precontraction | | Long precontraction | |
	Min R_λ	Max R_λ	Min R_λ	Max R_λ	Min R_λ	Max R_λ
R_{λ_a}	98.5	169.0	275	470	156	278
x_a/M	16.2	16.2	16.2	16.2	38.3	38.3
$\langle U_{1_a}\rangle$(m s^{-1})	2.10	4.37	2.38	4.76	2.34	4.74
$\langle u_{1_a}^2\rangle^{1/2}/\langle U_{1_a}\rangle$(%)	12.0	12.8	22.3	25.2	12.2	13.6
$\langle u_{1_a}^2\rangle^{1/2}/\langle u_{2_a}^2\rangle^{1/2}$	1.34	1.34	1.52	1.63	1.20	1.26
ℓ_a(cm)	3.86	5.13	14.2	18.3	8.60	12.0
λ_a (mm)	5.88	4.55	7.76	5.86	8.24	6.47
η_a (mm)	0.301	0.178	0.238	0.137	0.335	0.197
$\langle\epsilon_a\rangle$(m^2 s^3)	0.41	3.38	1.05	9.46	0.268	2.23
$\dfrac{\langle(\partial u_2/\partial x)^2\rangle}{\langle(\partial u_1/\partial x)^2\rangle}$	1.58	1.83	1.49	1.75	1.65	1.85

TABLE 1. Various initial flow parameters for: (a) passive grids with mesh lengths M of 2.54 cm and 5.08 cm and (b) the active grid with mesh length 5.08 cm. The short and the long precontraction lengths for the passive grid were 94.25 cm and 201.9 cm, respectively. The short and the long precontraction lengths for the active grid were 102.9 cm and 209.8 cm, respectively (see figure 1; subscript a, above, refers to the precontraction position). Here the integral length scale $\ell \equiv \langle u_1^2\rangle^{3/2}/\langle\varepsilon\rangle$ and the Kolmogorov length scale $\eta \equiv (\nu^3/\langle\varepsilon\rangle)^{1/4}$. A number of experiments were done at various speeds for each grid configuration. Here we only list the minimum and maximum speeds.

eliminate the effect of the acoustic mode on the flow, the longer precontraction was built (figure 1). It was found that the acoustic mode lost most of its energy after this modification. Figure 3 shows the one-dimensional energy spectrum of the longitudinal velocity component for the short and long precontraction lengths for the active grid (random mode), where the acoustic problem was most severe. The spectra have been scaled to match in the inertial range. (Note that their slope is less than $-5/3$. This is a Reynolds-number effect (Mydlarski & Warhaft 1996).) The inset in figure 3 shows κ_1 times the energy spectra, which gives the energy per bandwidth in wavenumber space. The acoustic peak is almost negligible for the long precontraction case. Although highly pronounced, we shall show below that the acoustic mode does not affect the postcontraction results significantly, by comparing results from the short and long precontraction-length runs.
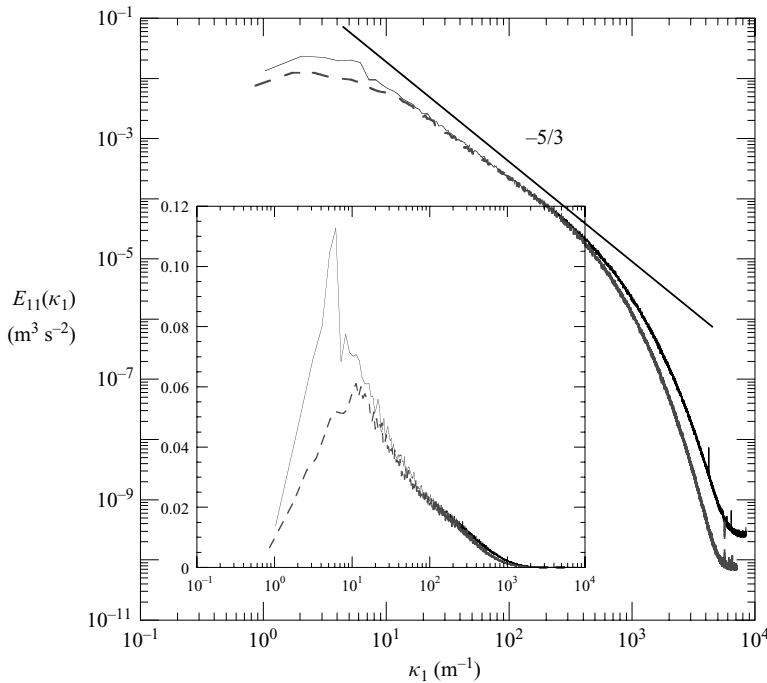
$E_{11}(\kappa_1)$
$(\text{m}^3 \text{ s}^{-2})$

FIGURE 3. Noise comparsion: solid black line, random grid with short initial test section (RS), $R_{\lambda_a} = 280$; dashed grey line, random grid with long initial test section (RL), $R_{\lambda_a} = 160$. Inset shows the spectra multiplied by κ_1. The slopes of the spectra are approximately -1.51.

Table 1 summarizes some typical flow conditions and characteristic values at measurement station a, before the contraction (figure 1).

4. Results

4.1. *Parameter variation*

As discussed in section 2, for the particular contraction geometry used, our flow is uniquely parameterized by $\overline{S}^*$, R_{λ_a} and the initial anisotropy $\langle u_{1_a}^2 \rangle^{1/2}/\langle u_{2_a}^2 \rangle^{1/2}$. Figure 4(a), shows the variation in $\overline{S}^*$ with R_{λ_a} for the various flow conditions of table 1 (subscript a indicates the measurement station just before the contraction†). The parameters were varied by using the different grids, different precontraction lengths and different mean speeds. The variation in $\overline{S}^*$ with initial variance anisotropy $\langle u_{1_a}^2 \rangle^{1/2}/\langle u_{2_a}^2 \rangle^{1/2}$ is shown in figure 4(b).

From figures 4(a) and 4(b) we can see the presence of two distinct groups in the parameter space, a moderate strain-rate group comprising measurements made in the

---

† For some cases (1PS, 2PS, SS and RS; see figure 4) the measurement station a was as much as 25 cm before the contraction (see figure 6 for typical measurement positions). We note that in the immediate precontraction region the flow speeds up and the variances increase. Ideally the position a should be just before this region, which changes as a function of the flow conditions. Because of the fixed location of the measuring ports we were unable to make fine adjustments of position a for each experiment. In the figures we compare extrapolated measurements of various variance ratios with those actually measured upstream of the contraction. Errors due to the inexact upstream location will be discussed.
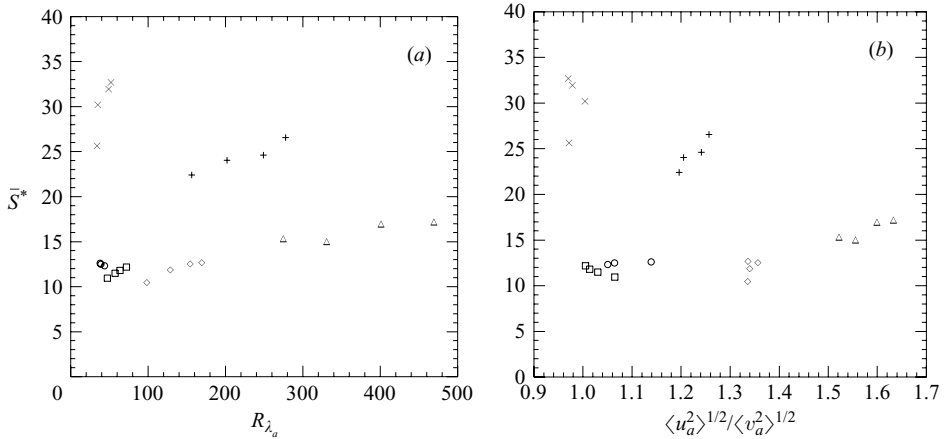
FIGURE 4. Variation of $\overline{S}^*$ as a function of (*a*) R_{λ_a} and (*b*) initial precontraction anisotropy: $\circ$, 2.54 cm passive grid, short precontraction (1PS); $\square$, 5.08 cm passive grid, short precontraction (2PS); $\diamond$, active grid, synchronous mode, short precontraction (SS); $\triangle$, active grid, random mode, short precontraction (RS); $\times$, 5.08 cm passive grid, long precontraction (2PL); $+$, active grid, random mode, long precontraction (RL).

short precontraction and a higher strain-rate group done with the long precontraction. The lower strain-rate group spans an R_{λ_a}-range of 40 to 470, over which $\overline{S}^*$ changes from 10 to 15, and the higher strain-rate group spans a smaller Reynolds-number range: R_{λ_a} varies from 40 to 300 as $\overline{S}^*$ changes from 20 to 35. The lower strain-rate group has some variation in initial anisotropy while the higher strain-rate group is nearly isotropic. For a particular grid and precontraction length $\overline{S}^*$ increases with R_{λ_a}, but no clear dependence of $\overline{S}^*$ on initial isotropy is observed (figure 4*b*).

4.2. *Effect of strain*

Within the contraction there is a variation in strain rate (figure 2*b*). This, coupled with the change in turbulence quantities as they evolve in the contraction causes a variation in S^* (2.3). Figure 5 shows S^* in the contraction for $R_\lambda = 44$, passive grid, and $R_\lambda = 260$, active grid. For both cases S^* varies from 10 to 100. Although there is approximately an order of magnitude variation, its value remains in an intermediate range, far from the rapid limit ($S^* \ll \infty$). The combination of the inhomogenity and the intermediate value of S^* strictly precludes the use of the form of the RDT as employed here. Our objective is to use this theory as a reference framework only. The strain rate when normalized with small time scales ($S\tau_\eta$, figure 5) was also determined. Notice the large difference, of two orders or more in magnitude, between S^* and $S\tau_\eta$, indicating that the strain effects on the large and small scales are vastly different. It is this difference, rather than the relatively weak variation in the strain rate, that we believe gives rise to the interesting dynamics to be discussed below.

Figure 6 shows the change in the root-mean-square velocity fluctuations normalized by $\langle U_{1_a} \rangle$ as a function of the downstream distance x_1, for various representative cases (table 1). The strain causes the longitudinal (x_1-direction) root-mean-square velocity fluctuations $\langle u_1^2 \rangle^{1/2}$ to be suppressed and the transverse (x_2-direction) r.m.s. velocity fluctuations $\langle u_2^2 \rangle^{1/2}$ to be amplified (Uberoi 1956; Mills & Corrsin 1959; Warhaft 1980). The various pre- and postcontraction parameters are listed in table 2. From figure 6 it can be determined that the precontraction ratio $\langle u_{1_a}^2 \rangle^{1/2} / \langle u_{2_a}^2 \rangle^{1/2}$ varies
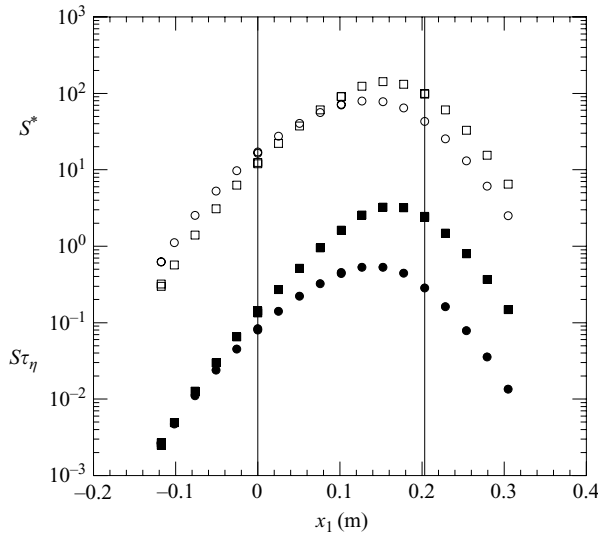
FIGURE 5. Normalized strain rate as a function of the downstream distance measured from the contraction. Open symbols, S^*; filled symbols, $S\tau_\eta$. Squares, $R_\lambda = 44$, 2.54-cm-mesh passive grid, short precontraction; circles, $R_\lambda = 260$, 5.08-cm-mesh active grid random mode, long precontraction. The vertical lines are the location of the contraction.

from the isotropic value of unity (figure 6b) to about 1.7 (figure 6f) (see also figure 7c). We will examine the consequences of this below. Also note that for these plots (made using dimensional downstream distances), the slow return to isotropy for the passive grids at low Reynolds numbers (figures 6a, 6b and 6c) compared with the higher-Reynolds-number active grids (figures 6d, 6e and 6f). We will present normalized data below.

In figure 7(a) the ratio of r.m.s. velocity fluctuations before and after the contraction for the longitudinal fluctuations u_1 and the transverse fluctuations u_2 as a function of $\overline{S}^*$ are shown (See table 2 for representative values). These ratios are also plotted as functions of R_{λ_a} and of initial anisotropy in figures 7(b) and 7(c) respectively. The transverse r.m.s. ratio is around 1.5 and the longitudinal ratio is around 0.5 (with a possible weak dependence on $\overline{S}^*$). The ratios $\langle u_{2_b}^2 \rangle^{1/2}/\langle u_{2_a}^2 \rangle^{1/2}$ and $\langle u_{1_b}^2 \rangle^{1/2}/\langle u_{1_a}^2 \rangle^{1/2}$ appear to be independent of R_{λ_a} and the initial anisotropy $\langle u_{1_a}^2 \rangle^{1/2}/\langle u_{2_a}^2 \rangle^{1/2}$, except perhaps for $R_{\lambda_a} \leqslant 100$. The horizontal lines in the figure are the RDT limits of 1.75 and 0.45 for an initial isotropic spectrum (Ribner & Tucker 1953). Evidently the longitudinal r.m.s. fluctuation ratio agrees well with the RDT prediction. The agreement for the transverse prediction is less good, particularly for the low-strain high-Reynolds-number experiments, the case where we might have expected the largest departure. As footnoted earlier, some of the precontraction measurements were made relatively far upstream of the physical contraction. In figures 7(a), 7(b) and 7(c) we have extrapolated these to the immediate precontraction region, and the results compare better with RDT.

Figure 8 shows a plot of the small-scale postcontraction (station b) anisotropy, $\langle (\partial u_{2_b}/\partial x_1)^2 \rangle/\langle (\partial u_{1_b}/\partial x_1)^2 \rangle$, as a function of the precontraction Reynolds number R_{λ_a}. The inset shows the small-scale precontraction anisotropy ratio at station a. It is close to the isotropic value of 2 for all cases. After the flow emerges from the contraction, if the Reynolds number of the turbulence entering the contraction is high then the
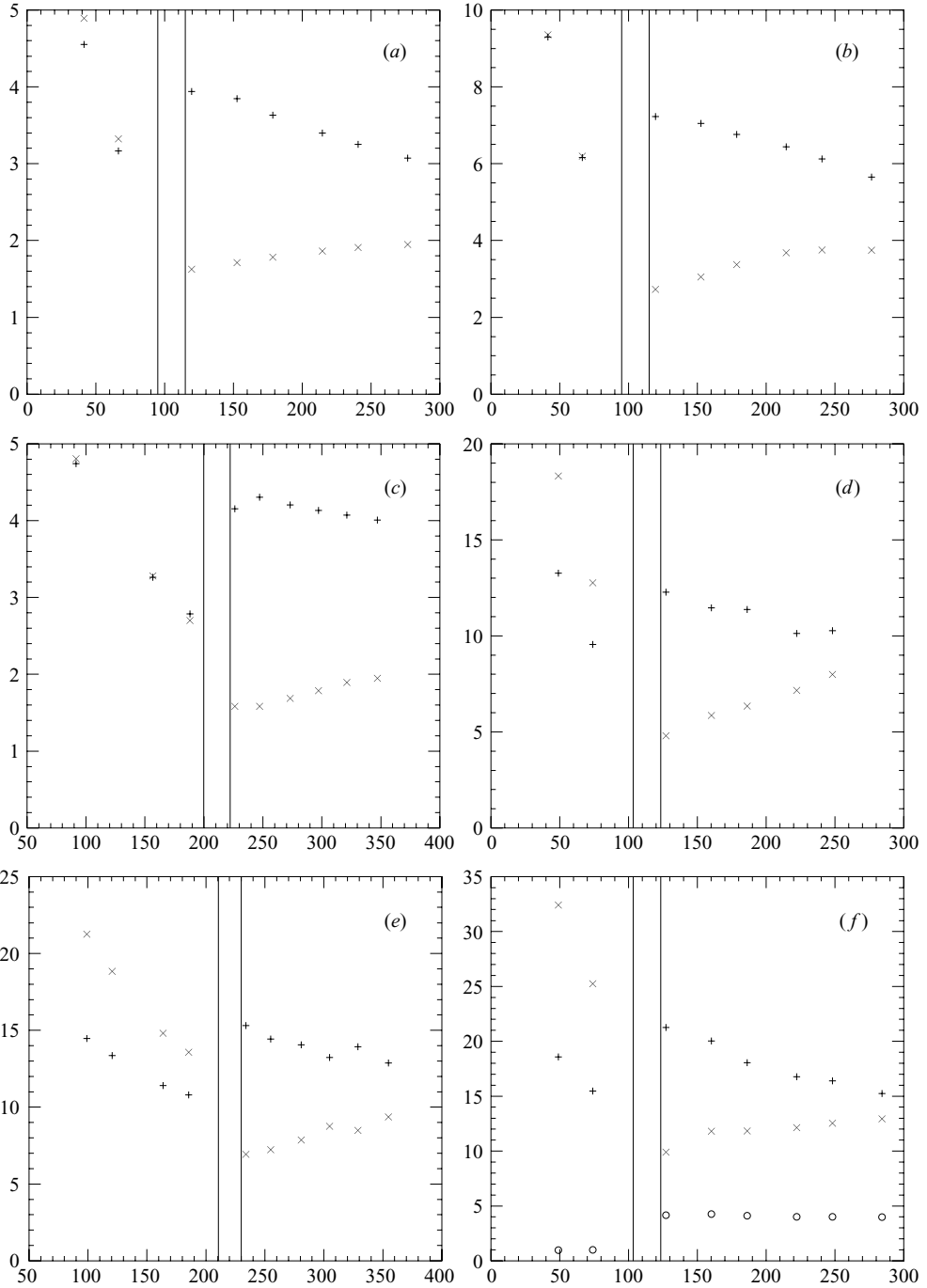
FIGURE 6. Variation of $\langle u_1^2 \rangle^{1/2} / \langle U_{1_a} \rangle$ (%) ($\times$) and $\langle u_2^2 \rangle^{1/2} / \langle U_{1_a} \rangle$ (%) (+) with downstream distance x (cm): (a) 2.54 cm passive grid, short precontraction (1PS), $R_{\lambda_a} = 44$; (b) 5.08 cm passive grid, short precontraction (2PS), $R_{\lambda_a} = 72$; (c) 5.08 cm passive grid, long precontraction (2PL), $R_{\lambda_a} = 52$; (d) active grid, synchronous mode, short precontraction (SS), $R_{\lambda_a} = 170$; (e) active grid, random mode, long precontraction (RL), $R_{\lambda_a} = 277$; (f) active grid, random mode, short precontraction (RS), $R_{\lambda_a} = 470$. Vertical lines represent the location of the contraction.
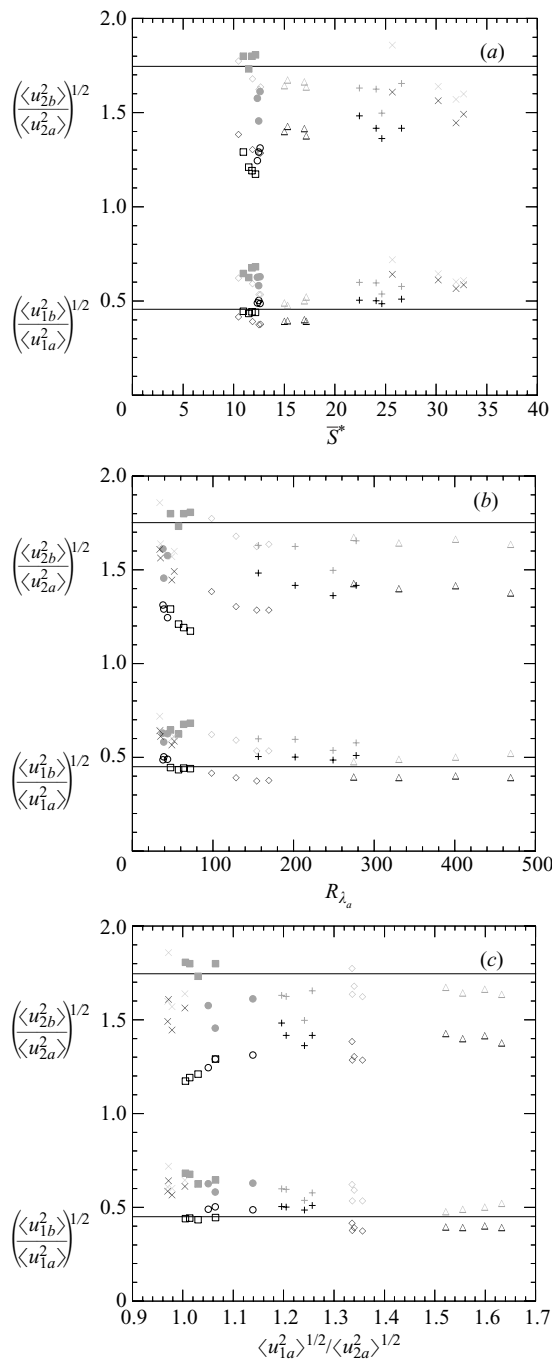
FIGURE 7. Variation of post- to precontraction r.m.s. ratios $(\langle u_{2_b}^2 \rangle / \langle u_{2_a}^2 \rangle)^{1/2}$ and $(\langle u_{1_b}^2 \rangle / \langle u_{1_a}^2 \rangle)^{1/2}$: (a) as a function of $\overline{S}^*$; (b) as a function of R_{λ_a}; (c) as a function of initial precontraction anisotropy. Subscripts a and b refer to the pre- and postcontraction regions respectively. The grey symbols are extrapolations of the precontraction variances to the immediate precontraction region (see text). The black symbols are from the actual measurements. The horizontal lines are the RDT predictions for an initial isotropic spectrum. The symbols have the same meaning as in figure 4.

(a)	Passive, $M = 2.54$ cm		Passive, $M = 5.08$ cm			
	Short precontraction		Short precontraction		Long precontraction	
	Min R'_λ	Max R'_λ	Min R'_λ	Max R'_λ	Min R'_λ	Max R'_λ
R'_{λ_b}	133	159	179	224	173	226
$\overline{S}^*$	7.28	7.12	6.33	7.02	17.4	18.9
$\langle u^2_{1_b}\rangle^{1/2}/\langle U_{1_b}\rangle$ (%)	0.400	0.400	0.586	0.617	0.379	0.379
$\langle u^2_{1_b}\rangle^{1/2}/\langle u^2_{1_a}\rangle^{1/2}$	0.487	0.489	0.445	0.440	0.612	0.586
$\langle u^2_{2_b}\rangle^{1/2}/\langle u^2_{2_a}\rangle^{1/2}$	1.31	1.24	1.29	1.17	1.56	1.49
k_b (m^2 s^2)	0.0192	0.0452	0.0318	0.130	0.0102	0.0427
ℓ'_b (cm)	15.6	14.5	22.0	17.1	36.3	30.2
$\langle\epsilon'_b\rangle$ (m^2 s^3)	0.0093	0.0362	0.0140	0.148	0.0154	0.0159
$\dfrac{\langle(\partial u_{2_b}/\partial x)^2\rangle}{\langle(\partial u_{1_b}/\partial x)^2\rangle}$	3.09	2.63	2.82	2.29	4.26	3.12

(b)	Synchronous mode		Random mode			
	Short precontraction		Short precontraction		Long precontraction	
	Min R'_λ	Max R'_λ	Min R'_λ	Max R'_λ	Min R'_λ	Max R'_λ
R'_{λ_b}	202	254	289	372	327	412
$\overline{S}^*$	6.04	7.31	8.85	9.92	29.3	15.8
$\langle u^2_{1_b}\rangle^{1/2}/\langle U_{1_b}\rangle$ (%)	1.08	1.07	2.19	2.38	1.50	1.68
$\langle u^2_{1_b}\rangle^{1/2}/\langle u^2_{1_a}\rangle^{1/2}$	0.416	0.377	0.395	0.392	0.504	0.510
$\langle u^2_{2_b}\rangle^{1/2}/\langle u^2_{2_a}\rangle^{1/2}$	1.38	1.28	1.43	1.38	1.48	1.42
k_b (m^2 s^2)	0.0732	0.310	0.27	1.137	0.260	0.539
ℓ'_b (cm)	18.6	14.2	19.7	15.9	35.7	27.3
$\langle\epsilon'_b\rangle$ (m^2 s^3)	0.058	0.659	0.388	4.15	0.0756	0.884
$\dfrac{\langle(\partial u_{2_b}/\partial x)^2\rangle}{\langle(\partial u_{1_b}/\partial x)^2\rangle}$	2.18	2.02	1.94	1.99	2.14	2.04

TABLE 2. Various flow parameters and post- to precontraction ratios: (*a*) passive grids; (*b*) active grids. The post- to precontraction velocity ratio was 4. Here $\langle\epsilon'_b\rangle \equiv 5\nu(\langle(\partial u_{1_b}/\partial x)^2\rangle + \langle(\partial u^2_{2_b}/\partial x)^2\rangle)$ and $\ell'_b \equiv (\frac{1}{3}\langle u^2_{1_b}\rangle + \frac{2}{3}\langle u^2_{2_b}\rangle)^{3/2}/\langle\epsilon'_b\rangle$. The subscript b refers to the immediate postcontraction region (figure 1).

effect of the strain on the small-scale isotropy is small. Thus for $R_{\lambda_a} \geqslant 150$, the postcontraction small-scale ratio is at the isotropic value of 2. The preferential effect of the strain on the large scales is due to the non-rapidness of the distortion, and the profound consequences for the future evolution of the flow will be examined in the second part of the study. If the strain were instantaneous (rapid distortion) then the small-scale derivative variance ratio would be approximately 7 for $c = 4$ (the exact value is slightly dependent on the form of the dissipation spectrum). The maximum value obtained in this experiment was 4.25 (figure 8). In these experiments we achieved comparatively greater variation in R_λ than in $\overline{S}^*$ but presumably if we could effect a larger variation in $\overline{S}^*$ we would find comparable differences in the response of the large and small scales to the strain rate, for a fixed Reynolds number.

   Figure 9 shows the effect of the strain on the postcontraction Reynolds number. Because the anisotropy produced by the strain can affect the dissipation scales, a definition of the Taylor Reynolds number R_λ that incorporates both the x_1 and x_2 directional quantities is required. We define the immediate postcontraction Reynolds

(a)		Passive, $M = 2.54$ cm		Passive, $M = 5.08$ cm			
		Short precontraction		Short precontraction		Long precontraction	
		Min R_λ	Max R_λ	Min R_λ	Max R_λ	Min R_λ	Max R_λ
Meas. station	R_{λ_a}	38.2	43.8	47.3	72	34.9	52.1
station a	$-S_{\partial u_1/\partial x_1}$	0.44	0.41	0.46	0.40	0.47	0.44
station b	$-S_{\partial u_1/\partial x_1}$	-0.014	-0.07	-0.13	-0.13	0.11	-0.08
station a	$K_{\partial u_1/\partial x_1}$	4.01	4.05	4.30	4.48	4.21	4.40
station b	$K_{\partial u_1/\partial x_1}$	5.14	5.20	6.07	5.83	5.28	6.30
station a	$K_{\partial u_2/\partial x_1}$	4.92	4.94	5.40	5.55	5.32	5.62
station b	$K_{\partial u_2/\partial x_1}$	5.39	5.61	6.46	6.70	5.28	6.34

(b)		Synchronous mode		Random mode			
		Short precontraction		Short precontraction		Long precontraction	
		Min R_λ	Max R_λ	Min R_λ	Max R_λ	Min R_λ	Max R_λ
Meas. station	R_{λ_a}	98.5	169.0	275	470	156	278
station a	$-S_{\partial u_1/\partial x_1}$	0.46	0.42	0.53	0.44	0.52	0.47
station b	$-S_{\partial u_1/\partial x_1}$	-0.25	-0.18	-0.04	0.03	-0.24	-0.11
station a	$K_{\partial u_1/\partial x_1}$	5.19	5.69	8.69	9.28	7.63	8.66
station b	$K_{\partial u_1/\partial x_1}$	10.7	8.79	11.4	10.4	15.1	13.5
station a	$K_{\partial u_2/\partial x_1}$	6.57	6.92	10.7	10.8	10.2	10.9
station b	$K_{\partial u_2/\partial x_1}$	12.6	12.2	18.3	14.5	19.9	18.8

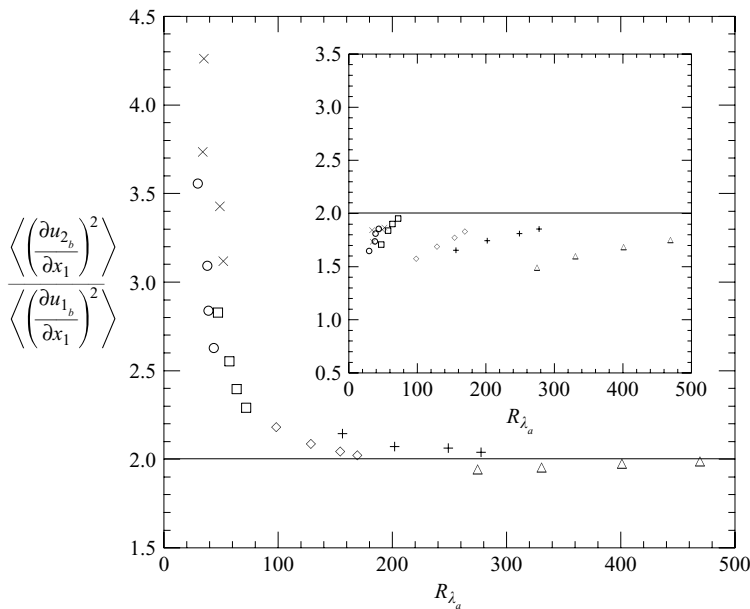TABLE 3. Skewness and kurtosis of velocity derivatives. (*a*) Passive grids; (*b*) active grids.

FIGURE 8. Variation of post-contraction small-scale anisotropy with R_{λ_a}. The inset shows the precontraction small-scale isotropy. The symbols have the same meaning as in figure 4.
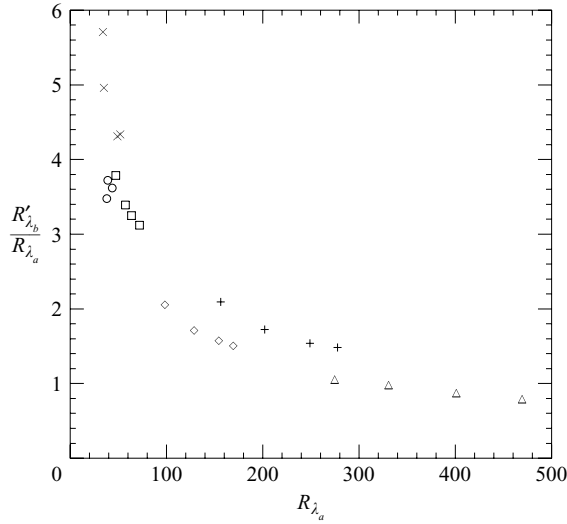
FIGURE 9. Variation of $R'_{\lambda_b}/R_{\lambda_a}$ (see text) with R_{λ_a}. The symbols have the same meaning as in figure 4.

number R'_λ as

$$R'_\lambda = \sqrt{\frac{u_1^2 + 2u_2^2}{3}} \frac{\lambda'}{v} \tag{4.1}$$

where λ' is defined as

$$\lambda' = \langle U_1 \rangle \sqrt{\frac{u_1^2 + 2u_2^2}{(\partial u_1/\partial t)^2 + (\partial u_2/\partial t)^2}}. \tag{4.2}$$

The ratio $R'_{\lambda_b}/R_{\lambda_a}$ when plotted as a function of R_{λ_a} (figure 9) approaches a limit of approximately 1 for the highest Reynolds numbers. Note that this ratio is dominated by the small scales, since the values of the r.m.s. velocities are approximately the same for all the experiments described here (figures 7a and 7b). Thus figure 9 is similar to figure 8.

We now turn to spectra. Figures 10(a) and 10(b) show one-dimensional u_1 and u_2 energy spectra, $E_{11}(\kappa_1)$ and $E_{22}(\kappa_1)$, at low Reynolds number ($R_{\lambda_a} = 44$) and low strain rate ($\overline{S}^* = 12$), before and after the contraction. The insets show the energy spectra multiplied by κ_1. Similarly, figure 11 shows energy spectra at high Reynolds number ($R_{\lambda_a} = 260$) but still with a relatively low strain rate ($\overline{S}^* = 24$) and figure 12 shows energy spectra at low Reynolds number ($R_{\lambda_a} = 50$) but now at a higher strain rate ($\overline{S}^* = 32$) than in figure 10. Also shown in figures 10, 11 and 12 are isotropic model spectra in the precontraction region, and the corresponding distorted spectra calculated using RDT. The postcontraction spectra have been plotted using a scaled wavenumber (c times the postcontraction wavenumber, (2.28)), and the spectra have been normalized by the same factor c. This is to ensure that we compare the energy of the same wave modes in physical space. In all cases (figures 10, 11 and 12) the strain suppresses the large scales in the longitudinal direction and amplifies them in the transverse direction. (This is also evident for the r.m.s. values (figure 7).) From the energy per bandwidth spectra (see the insets of figures 10, 11 and 12), we observe that the spectrum-peak shifts to higher wavenumbers for the longitudinal case and does
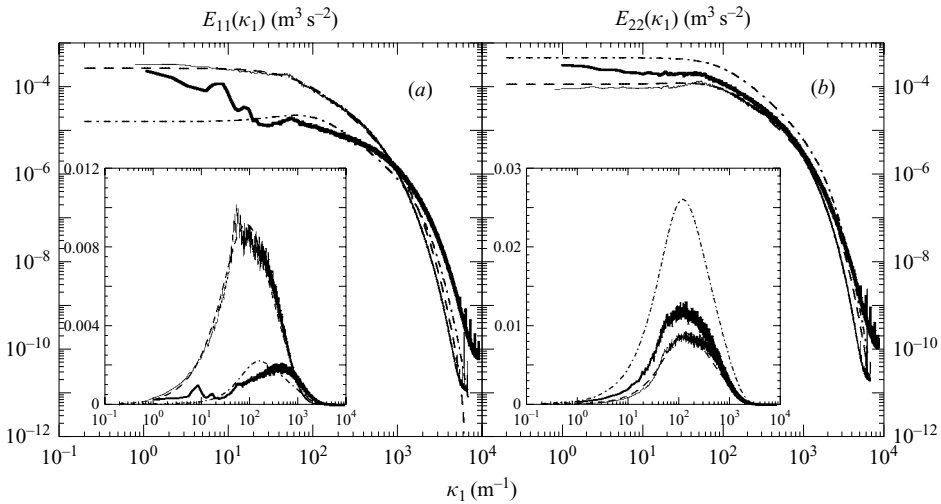
$E_{11}(\kappa_1)$ (m^3 s^{-2}) $E_{22}(\kappa_1)$ (m^3 s^{-2})

FIGURE 10. One-dimensional energy spectra, 2.54 cm passive grid, short precontraction (1PS), $R_{\lambda_a} = 44$, $\overline{S}^* = 12$. (a) $E_{11}(\kappa_1)$, inset $\kappa_1 E_{11}(\kappa_1)$; (b) $E_{22}(\kappa_1)$, inset $\kappa_1 E_{22}(\kappa_1)$. Thin black line, station a experiment; dashed line, station a model spectrum. Thick black line, station b experiment; dashed-dotted line, station b model spectrum. The postcontraction wavenumbers have been multiplied by c and the amplitudes of the spectra by $1/c$ (see text immediately following (equation 2.27)).

$E_{11}(\kappa_1)$ (m^3 s^{-2}) $E_{22}(\kappa_1)$ (m^3 s^{-2})
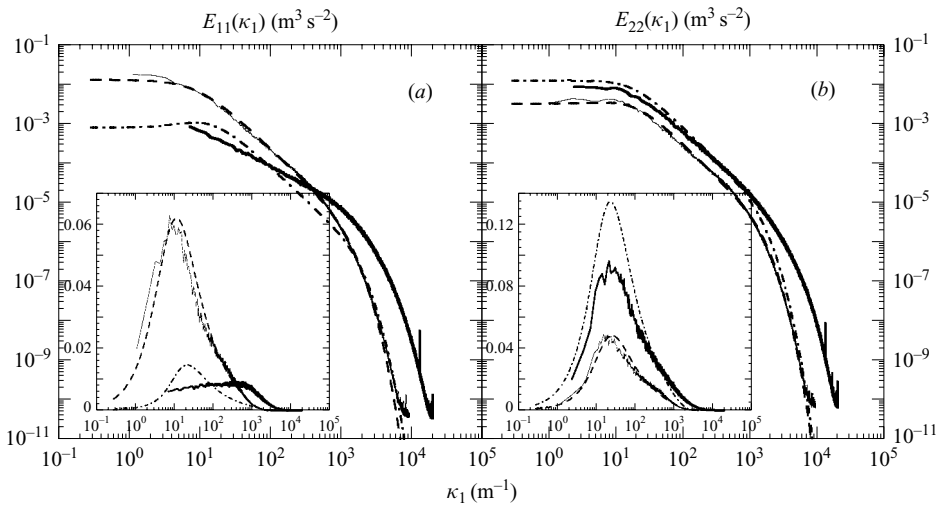
FIGURE 11. One-dimensional energy spectra, active grid, long precontraction (RL), $R_{\lambda_a} = 260$, $\overline{S}^* = 24$. (a) $E_{11}(\kappa_1)$, inset $\kappa_1 E_{11}(\kappa_1)$; (b) $E_{22}(\kappa_1)$, inset $\kappa_1 E_{22}(\kappa_1)$. Thin black line, station a experiment; dashed line, station a model spectrum. Thick black line, station b experiment; dashed-dotted line, station b model spectrum. The post-contraction wavenumbers have been multiplied by c and the amplitudes of the spectra by $1/c$.

not shift significantly for the transverse case. The shift in peak is more for the higher R_{λ_a} values: for $R_{\lambda_a} = 260$ (figure 11) the peak of the u_1-spectrum is at approximately $1000\,\mathrm{m}^{-1}$ while that of the u_2-spectrum is at $20\,\mathrm{m}^{-1}$ i.e. their ratio is $50:1$. On the one hand, the model-spectra RDT calculations agree with the experimental observations
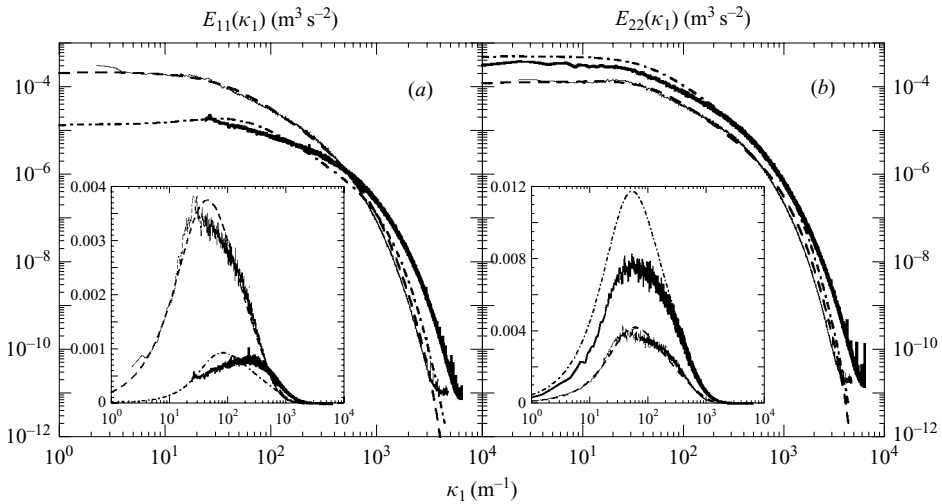
$E_{11}(\kappa_1)$ (m^3 s^{-2}) $E_{22}(\kappa_1)$ (m^3 s^{-2})

FIGURE 12. One-dimensional energy spectra, 5.08 cm passive grid, long precontraction (2PL), $R_{\lambda_a} = 50$, $\overline{S}^* = 32$: (a) $E_{11}(\kappa_1)$, inset $\kappa_1 E_{11}(\kappa_1)$; (b) $E_{22}(\kappa_1)$, inset $\kappa_1 E_{22}(\kappa_1)$. Thin black line, station a experiment; dashed line, station a model spectrum. Thick black line, station b experiment; dashed-dotted line, station b model spectrum. The post-contraction wavenumbers have been multiplied by c and the amplitudes of the spectra by $1/c$.

in terms of total energy for the longitudinal spectra and location of peak for the transverse spectra. On the other hand, RDT does not predict the shift in the peak of the longitudinal spectrum. It predicts that the longitudinal and transverse spectra should peak at approximately the same wavenumber (figures 10, 11 and 12). RDT also appears to overpredict the energy in the transverse strained spectrum. This is partly due to the precontraction measurement location (see below).

Owing to the presence of the acoustic peak, the highest-Reynolds-number cases (§2) have not been shown, but the trends are again consistent with the rest of the data sets. Thus for $R_{\lambda_a} = 470$ the peak of the strained longitudinal spectrum occurred at a wavenumber 200 times that of the transverse spectrum.

The mismatch in the peak wavenumber between the observations and the RDT calculations for the longitudinal spectra (figures 10, 11 and 12) is presumably due to the non-rapidness of the distortion or the non-uniformity of the strain rate within the contraction, or to a combination of both. We are inclined to think it is the former since, as noted with reference to figure 5, the effect of strain on the large and small scales is more salient than the variation of the strain rate in the contraction. (Viscous effects, not included in our calculations, would tend to inhibit the energy of the small scales. Our dissipation spectra (below) show the opposite effect: more energy is measured in the small scales than inviscid RDT predicts.) Rapid distortion theory is predicated on the assumption that turbulence–turbulence terms are negligible compared with the interaction of the turbulence and the mean strain (compare (2.6) and (2.9)) and this is clearly not the case in our experiments since S^* is in the range 10 to 100 inside the contraction (figure 5). If we consider the full equation for the evolution of ω_2, (2.8), the nonlinear term $\omega_1 \partial u_2 / \partial x_1$, because of the amplification of both ω_1 and $\partial u_2 / \partial x$, will enhance ω_2, producing additional u_1 fluctuations. These fluctuations will occur at higher wavenumbers because they involve correlations of turbulence–turbulence derivative terms as opposed to turbulence–mean-strain terms. The significance of this
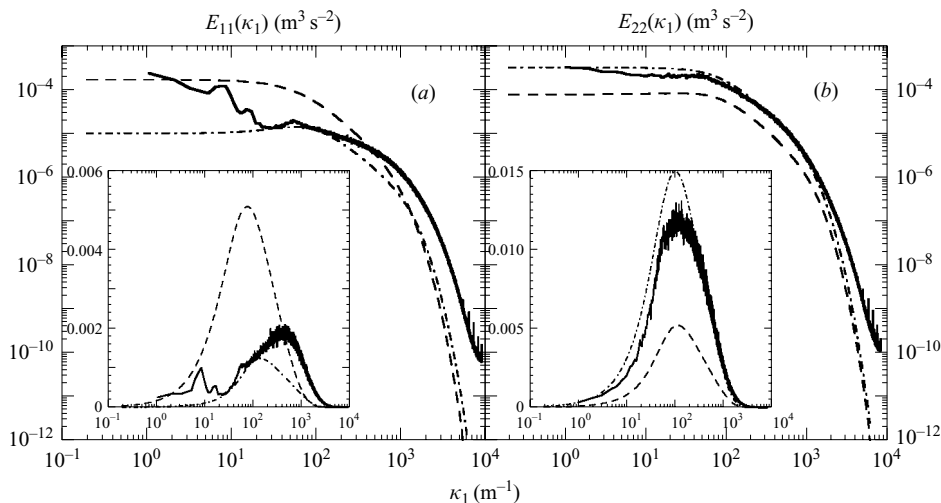
FIGURE 13. One-dimensional energy spectra, 2.54 cm passive grid, short precontraction (1PS), $R_{\lambda_a} = 44$, $\overline{S}^* = 12$. This is the same condition as shown in figure 10. Here the purpose is to compare with the RDT predictions made by extrapolating the data to the immediate precontraction region (see text). (a) $E_{11}(\kappa_1)$, inset $\kappa_1 E_{11}(\kappa_1)$; (b) $E_{22}(\kappa_1)$, inset $\kappa_1 E_{22}(\kappa_1)$. Dashed line, station a extrapolated model spectrum; thick black line, station b experiment; dashed-dotted line, station b extrapolated model spectrum. The postcontraction wavenumbers have been multiplied by c and the amplitudes of the spectra by $1/c$.

wavenumber shift, which is most pronounced at high Reynolds numbers (figure 11a), will become apparent when we study the postcontraction evolution.

The mismatch between the RDT predictions and the energy of the postcontraction transverse spectra (figures 10b, 11b and 12b) is mainly due to the precontraction positioning of the turbulence probe, discussed in relation to figure 7. As for figure 7, we have re-estimated the postcontraction spectra using RDT, by extrapolating the data in the precontraction to the immediate precontraction region. The results are shown in figure 13. The mismatch still remains but it is reduced considerably. However, there is now a mismatch between the amplitudes of RDT and the observed postcontraction longitudinal spectrum. Clearly these calculations are very sensitive to how the pre- and postcontraction locations are defined. Nevertheless, althrough RDT is in reasonable agreement with observations regarding amplitudes, it is always inconsistent with the location of the peak wavenumber of the longitudinal spectrum.

Typical longitudinal and transverse dissipation spectra are shown in figure 14. Their magnitudes are similar (figures 14a and 14b), indicating the tendency of small scales to return to isotropy, as was previously observed (figure 8). Also shown are the RDT calculations. Here, for the postcontraction region anisotropy is predicted at all wavenumbers, including the dissipation scales. As noted above, inviscid RDT under-predicts the high-wavenumber energy. Including viscosity in the calculations would increase the disparity with the experiments.

To illustrate the scale dependence of the return to isotropy, we plot the ratio of the longitudinal and the transverse one-dimensional spectra, $E_{11}(\kappa_1)/E_{22}(\kappa_1)$, as a function of wavenumber (figures 15a and 15b). These are the ratios of the measured low- and high-Reynolds-number spectra, shown in figures 10 and 11 respectively. The RDT calculations, also shown, are based on purely isotropic calculations that use the
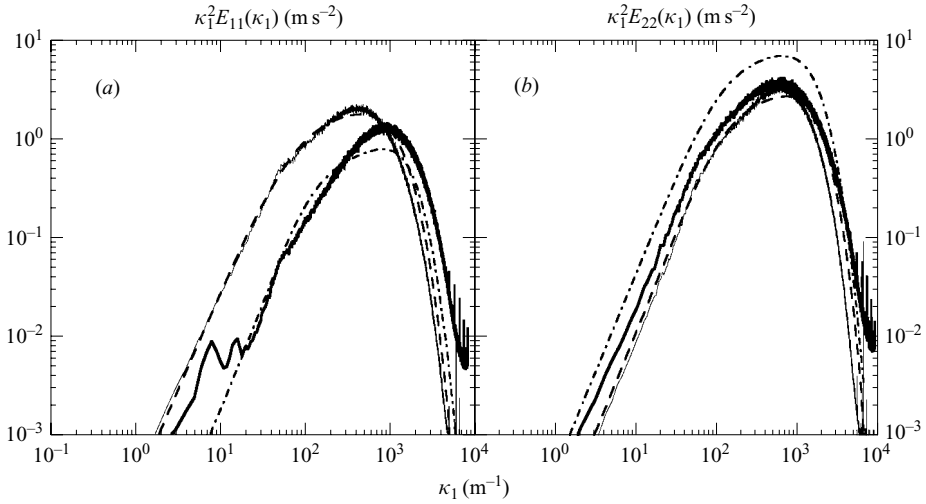
FIGURE 14. One-dimensional dissipation spectra, active grid, long precontraction (RL), $R_{\lambda_a} = 260$, $\overline{S}^* = 24$. (a) $\kappa_1^2 E_{11}(\kappa_1)$; (b) $\kappa_1^2 E_{22}(\kappa_1)$. Thin black line, station a experiment; dashed line, station a model spectrum; thick black line, station b experiment; dashed-dotted line, station b model spectrum. The post-contraction wavenumbers have been multiplied by c and the amplitudes of the dissipation spectra by $1/c^2$.
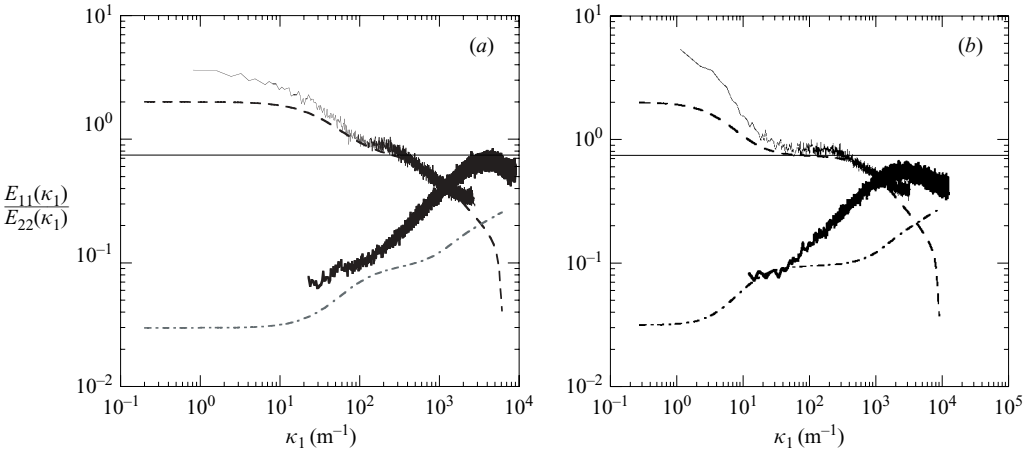
FIGURE 15. Energy-spectra ratio. (a) 2.54 cm passive grid, short precontraction (1PS), $R_{\lambda_a} = 44$, $\overline{S}^* = 12$; (b) active grid, long precontraction (RL), $R_{\lambda_a} = 260$, $\overline{S}^* = 24$. Thin black line, station a experiment; dashed line, station a model spectrum. Thick black line, station b experiment; dashed-dotted line, station b model spectrum. The post-contraction wavenumbers have been multiplied by c and the amplitudes of the spectra by $1/c$.

longitudinal fluctuation measurements as their input. The ratios provide insight into the effects of the distortion as a function of wavenumber. A property of isotropic turbulence spectra is that the ratios will increase with wavenumber in the near-to-far dissipation range (provided the spectra fall off faster than algebraically; we used an exponential), and this is observed for the model spectra and for the measurements in the precontraction regions, figure 15. The slight upturn in the precontraction measurements at the highest wavenumbers is due to noise. For the strained spectra,

however, RDT predicts that $E_{11}(\kappa_1)/E_{22}(\kappa_1)$ will increase with wavenumber (as before, the individual spectra have to have a faster-than-power-law decrease and this is satisfied by the form of the precontraction spectra), and the modelled results show this increase (figure 15) for high wavenumbers. The predicted increase is evident too in the measurements, but the ratio peaks and then begins to decrease at the highest wavenumbers. The wavenumber at which the peak occurs provides an indication of how far into the small scales the distortion is acting in the rapid sense. Beyond the peak the ratio exhibits the same tendency as the isotropic precontraction ratios, which is to decrease with increasing wavenumber. At these small scales the distortion has apparently had little effect. Note that the peak occurs at a relatively lower wavenumber (figure 15*b*) for the case farthest from rapid distortion (see figure 11), as would be expected. Note also that the measurements show a shift with regard to the RDT calculations. This is due to the fact that the longitudinal spectrum peaks at higher wavenumbers than the RDT prediction (figures 10 and 11) and also to the lower amplitude of the observed u_2-spectrum compared with RDT.

The results of figure 15 show that the strain, in the rapid sense, protrudes into the inertial subrange. It is instructive to determine a length scale at which the strain is as rapid as the turbulence time scale (Kevlahan & Hunt 1997). Using dimensional arguments, a length scale in the inertial range, ℓ_s, is associated with the time scale $\tau_s = \langle \varepsilon \rangle^{-1/3} \ell_s^{2/3}$. For the strain and turbulence to have the same time scale, $S\tau_s = 1$. The wavenumber κ_s corresponding to such a scale is $(10\pi/3\nu)\langle q_a^2 \rangle^{1/2} R_{\lambda_a}^{-2} (\overline{S}^*)^{3/2}$. The wavenumbers corresponding to the integral length scale ℓ and the Kolmogorov scale η are $\kappa_\ell = (10\pi/3\nu)\langle q_a^2 \rangle^{1/2} R_{\lambda_a}^{-2}$ and $\kappa_\eta = (2\pi/\nu)(5/3)^{1/4}\langle q_a^2 \rangle^{1/2} R_{\lambda_a}^{-1/2}$. Hence the ratios of wavenumbers scale as $(\kappa_s/\kappa_\ell) \sim (\overline{S}^*)^{3/2}$ and $(\kappa_s/\kappa_\eta) \sim (\overline{S}^*)^{3/2} R_{\lambda_a}^{-3/2}$. A typical measurement condition is for a Reynolds number of around 260 with a strain rate $\overline{S}^*$ of 24 (figure 15*b*). For this case the ratios are $\kappa_s/\kappa_\ell \sim 118$ and $\kappa_s/\kappa_\eta \sim 0.03$. The peak in energy is around $20\,\mathrm{m}^{-1}$ and the dissipation peak is around $1000\,\mathrm{m}^{-1}$ (nominally around 30η). This puts κ_s in the range $900\text{–}2000\,\mathrm{m}^{-1}$ and is consistent with the wavenumber at which isotropy effects are observed in the spectrum ratio (figure 13*b*). Thus, using this criterion the distortion is fast compared with the energy-containing scales as well as a significant part of the inertial-range scales. Further insightful discussion on the range of validity of RDT may be found in Kevlahan & Hunt (1997).

4.3. *Relaxation of strained turbulence*

The anisotropic turbulence created by the contraction relaxes towards isotropy (figure 6). Earlier (following (2.39)) we introduced a non-dimensional time coordinate s based on the integral time scale, $k/\langle \varepsilon \rangle$. In figure 16 we plot the relevant longitudinal and transverse components of the anisotropy tensor, b_{11} and b_{22} respectively, as a function of s. The Rotta model predicts an exponential decrease to zero (see §2.3) for these quantities, and experiments suggest that the Rotta constant C_R is in the range 1.8–2.6 (Hunt & Carruthers 1990). While an exponential function fits our data well, we find that C_R is not constant: for early times (figure 16*a*) its value is 5.5 while for later times it decreases to 2.6 (figure 16*b*). It is important to note that the results are independent of the grid type (active or passive) and also appear to be independent of Reynolds number.

In figure 17 we have plotted C_R as a function of the final value of s, defined as

$$s_f = \int_b^e \frac{k}{\langle \varepsilon \rangle} \frac{\mathrm{d}x_1}{\langle U_{1_b} \rangle} \tag{4.3}$$
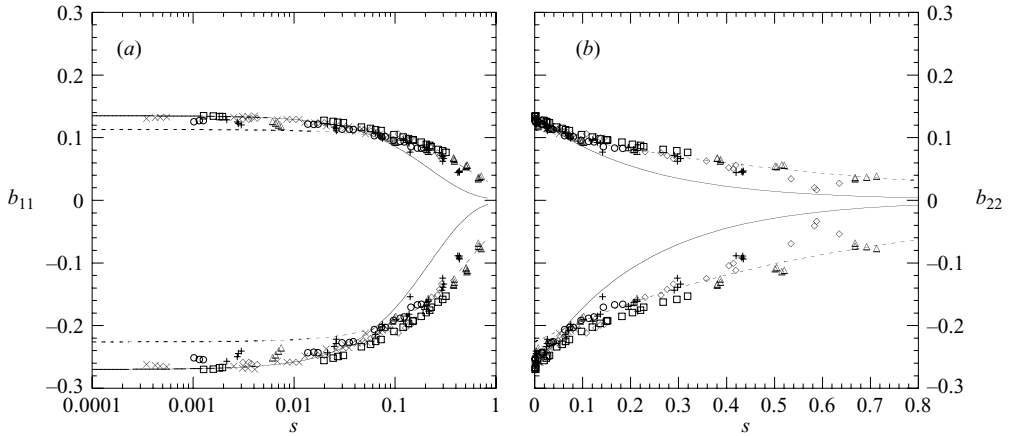
FIGURE 16. (a) The longitudinal and (b) transverse components b_{11} and b_{22} of the anisotropy tensor vs. s in the postcontraction section: solid line, exponential fit, $C_R = 5.5$; dashed line, exponential fit, $C_R = 2.6$. Symbols have the same meaning as in figure 4.
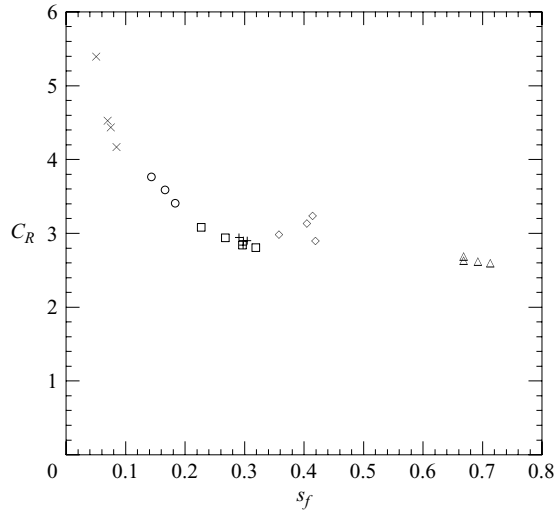

FIGURE 17. C_R (Rotta's constant) vs. s_f; symbols have the same meaning as in figure 4.

where e is the farthest downstream location at which the measurement was made. Here, C_R was calculated for each individual measurement set (i.e. for a fixed R_{λ_a} and $\overline{S}^*$). A variation in C_R with evolution time, at least to $s_f \sim 0.3$, is observed. After that the decrease is much slower and the results suggest an asymptotic value in the range 2.6–3. (Note that the active-synchronous-grid results ($s_f \sim 0.4$) tend to show, here and elsewhere, the greatest departure from the trends observed by the other grid results (static grids and the random active grid). But we have found no good reason to exclude them from our data set.) Our asymptotic value of $C_R \sim 2.8$ is consistent with other high-Reynolds-number determinations of this constant (Sjogren & Johansson 1998), and is also consistent with figure 16, where at short times the value is 5.5 and at long times around 2.8. Note that the asymptotic state occurs at a relatively modest Reynolds number ($R_{\lambda_a} \sim 150$, figure 17), but earlier work, cited in the introduction, was done at a very low Reynolds number, where the 'constant' was still evolving.
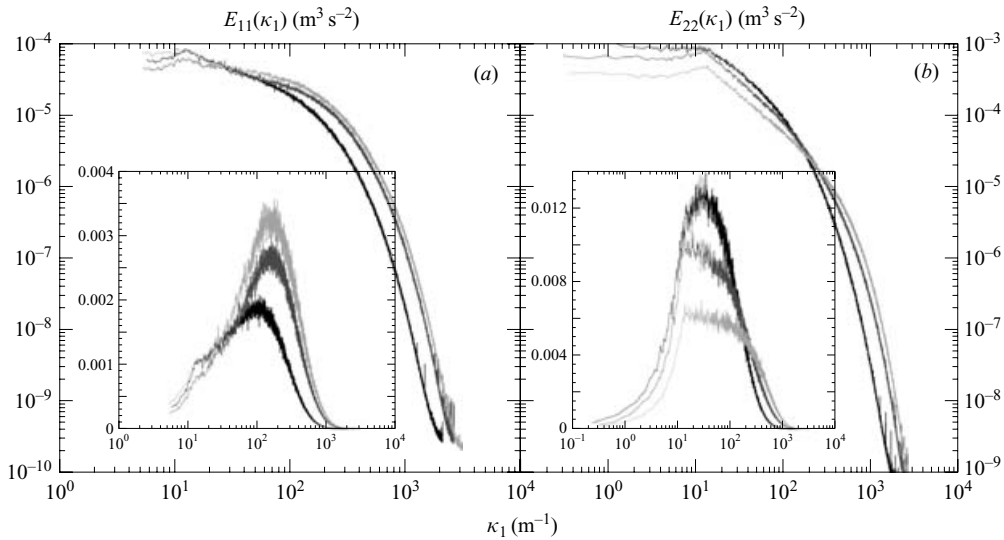
FIGURE 18. One-dimensional energy spectra, downstream evolution, 2.54 cm passive grid, short precontraction (1PS), $R_{\lambda_a} = 44$, $\overline{S}^* = 12$. (a) $E_{11}(\kappa_1)$, inset $\kappa_1 E_{11}(\kappa_1)$; (b) $E_{22}(\kappa_1)$, inset $\kappa_1 E_{22}(\kappa_1)$; black line, station b; dark grey line, intermediate station; light grey line, station e.
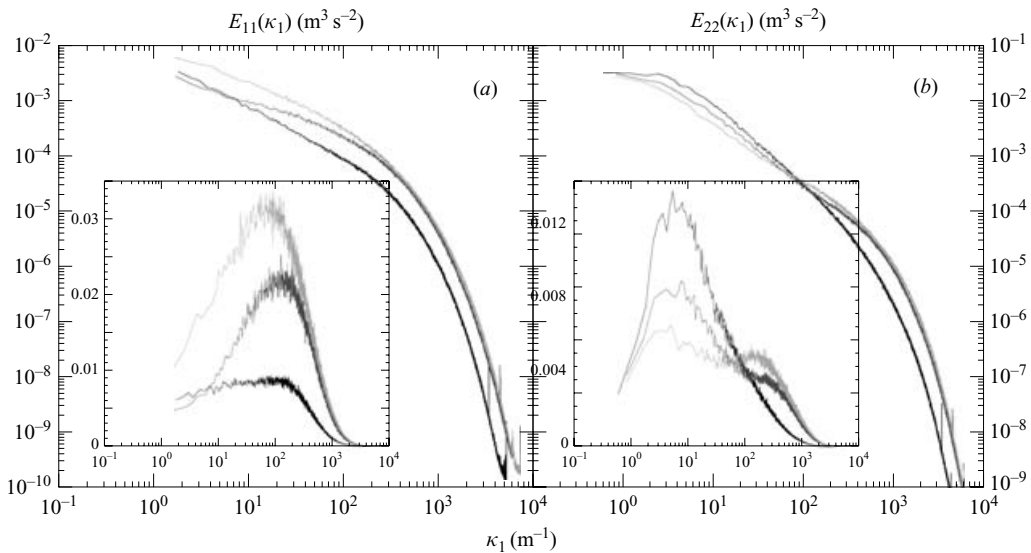

FIGURE 19. One-dimensional energy spectra, downstream evolution, active grid, long precontraction (RL), $R_{\lambda_a} = 260$, $\overline{S}^* = 24$. (a) $E_{11}(\kappa_1)$, inset $\kappa_1 E_{11}(\kappa_1)$; (b) $E_{22}(\kappa_1)$, inset $\kappa_1 E_{22}(\kappa_1)$; black line, station b; dark grey line, intermediate station; light grey line, station e.

We also considered some second-order return-to-isotropy models by including a quadratic term in b_{ij}. Here too the model constant had to be tuned as the Reynolds number changed.

We now turn to the evolution of the spectra in the postcontraction region. Figures 18 and 19 give one-dimensional energy spectra for low and high Reynolds numbers corresponding to the same initial conditions as the data presented in figures 10 and 11

respectively. (In these and in the postcontraction spectra to follow, we have not multiplied the wavenumber, κ_1, by c (as in figures 10–15) since here we are not comparing pre- and postcontraction spectra.) In both cases the longitudinal spectra (figures 18a and 19a; the insets give the energy per bandwidth) show an increase in energy as the flow evolves downstream, while the transverse spectra show the expected decrease (figure 6). But the disparity in the wavenumbers at which the longitudinal and transverse strained spectra ($E_{11}(\kappa_1)$ and $E_{22}(\kappa_1)$) emerge from the contraction peak (figures 10 and 11) causes them to undergo a complex evolution with downstream distance. At low Reynolds number (figure 18) there is a broadening of $E_{22}(\kappa_1)$ as the high-wavenumber energy in $E_{11}(\kappa_1)$ grows and interacts with the low-wavenumber transverse fluctuations. At the higher Reynolds numbers (figure 19) this occurs too, but the difference in the wavenumbers of the peak energy of the strained longitudinal and transverse spectra emerging from the contraction is so great that as the flow evolves, and the energy in the longitudinal fluctuation increases, a double peak occurs in the transverse spectrum with the higher peak, at approximately the same wavenumber as the peak in the longitudinal spectrum. Thus for both low and high Reynolds numbers there is a complex nonlinear interaction between the longitudinal and transverse fluctuations but it is most clearly manifest at high Reynolds numbers, where the difference in the wavenumbers at which the strained longitudinal and transverse spectra peak is most pronounced. Note that at the furthest downstream location (station e) there is approximate isotropy in terms of the longitudinal and transverse total energy (the integral of the spectra, figures 18 and 19), but as noted the distribution in energy is quite different, the transverse spectrum exhibiting a much broader distribution.

In order to compare further how the spectra vary with Reynolds number, in figure 20 we have plotted the energy per bandwidth spectra for the longitudinal and transverse components ($\kappa_1 E_{11}(\kappa_1)$ and $\kappa_1 E_{11}(\kappa_1)$), normalized by their respective peak energies, for the furthest downstream location and for the full variation of Reynolds numbers studied. Although these spectra are measured at the same downstream location, the evolved time (in integral-time-scale units) is greater for the higher Reynolds numbers. The longitudinal spectra broaden, as expected, with increasing Reynolds number. So do the transverse spectra, and the composite plots clearly illustrate the emergence of the double peak at high Reynolds number. It is remarkable that the progression from low to high Reynolds numbers was obtained by using quite different grids. The fact that the variation is so consistent suggests that the particular grid geometry does not have a pronounced effect on the subsequent evolution of the flow. It seems to be governed by the Reynolds number (and possibly to a small extent by the normalized strain, which was varied over only a modest range).

The broadening of the transverse spectra and the emergence of the double peak at high Reynolds number (figures 18, 19 and 20) indicate that there are long-range nonlinear interactions occurring in the flow. They occur because of the modulated distortion of the various scales, from almost rapid distortion for the largest scales to essentially no distortion at all for the smallest scales. The effect is most pronounced at high Reynolds number because of the broader initial spectrum.

The dissipation spectra corresponding to the energy spectra of figures 18 and 19 are shown in figures 21 and 22 respectively. Although the turbulent kinetic energy decreases with downstream distance for the transverse component (Figures 6, 18b, and 19b), the dissipation rate increases, owing to spectral transfer to the high wavenumbers. Both at low and high Reynolds numbers (figures 21b and 22b) the transverse dissipation spectra show extended approximately power-law regions for
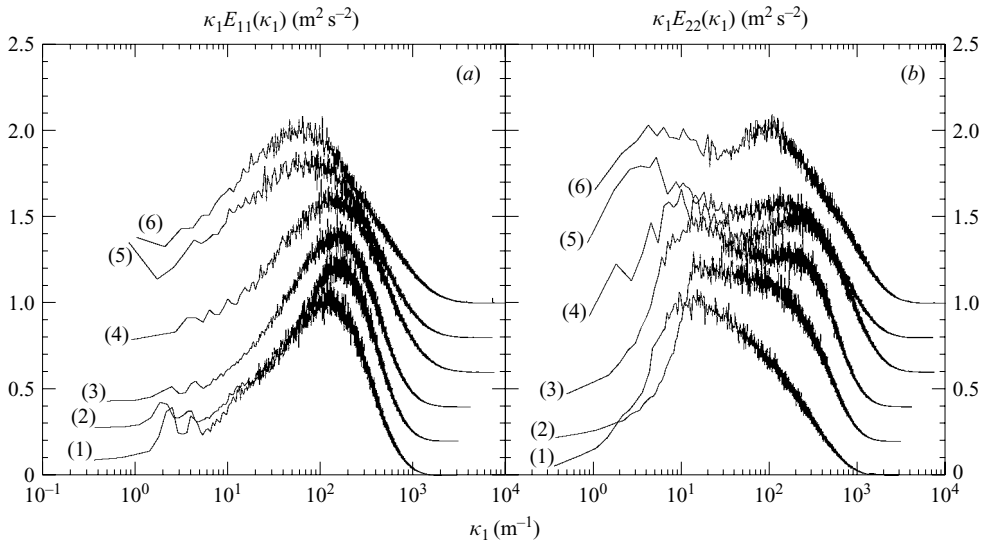
FIGURE 20. Normalized one-dimensional energy spectra, measured at the furthest location (station e) in the postcontraction region. (1) 5.08 cm passive grid, long precontraction (2PL), $R_{\lambda_1} = 52$, $\overline{S}^* = 32$; (2) 2.54 cm passive grid, long precontraction (1PS), $R_{\lambda_1} = 44$, $\overline{S}^* = 12$; (3) 5.08 cm passive grid, short precontraction (2PS), $R_{\lambda_1} = 64$, $\overline{S}^* = 12$; (4) active grid, synchronous mode, short precontraction (SS), $R_{\lambda_1} = 170$, $\overline{S}^* = 12.5$; (5) active grid, random mode, long precontraction (RL), $R_{\lambda_1} = 260$, $\overline{S}^* = 24$; (6) active grid, random mode, short precontraction (RS), $R_{\lambda_1} = 470$, $\overline{S}^* = 17$.
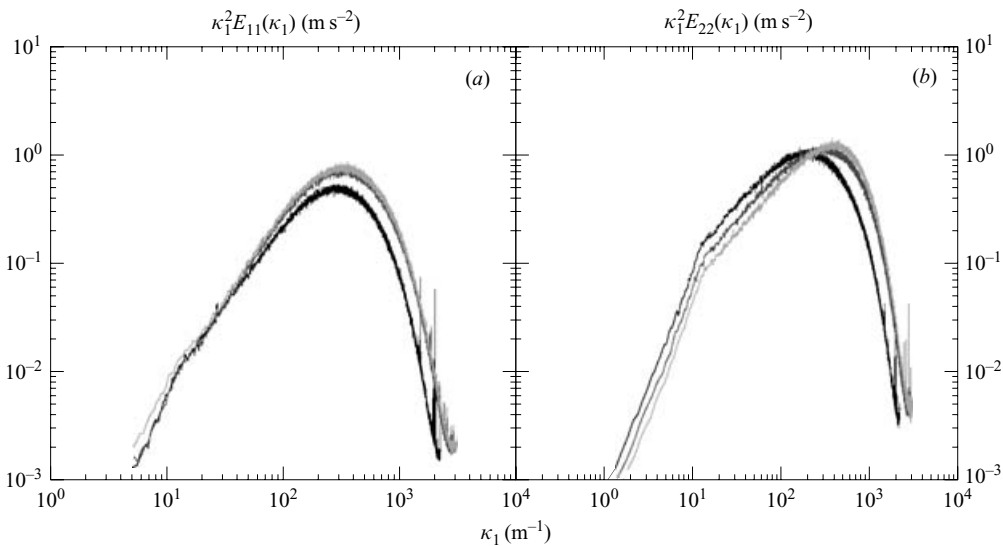

FIGURE 21. One-dimensional dissipation spectra, downstream evolution, 2.54 cm passive grid, short precontraction (1PS), $R_{\lambda_a} = 40$, $\overline{S}^* = 12$. (a) $\kappa_1^2 E_{11}(\kappa_1)$; ($b$) $\kappa_1^2 E_{22}(\kappa_1)$; black line, station b; dark grey line, intermediate station; light grey line, station e.
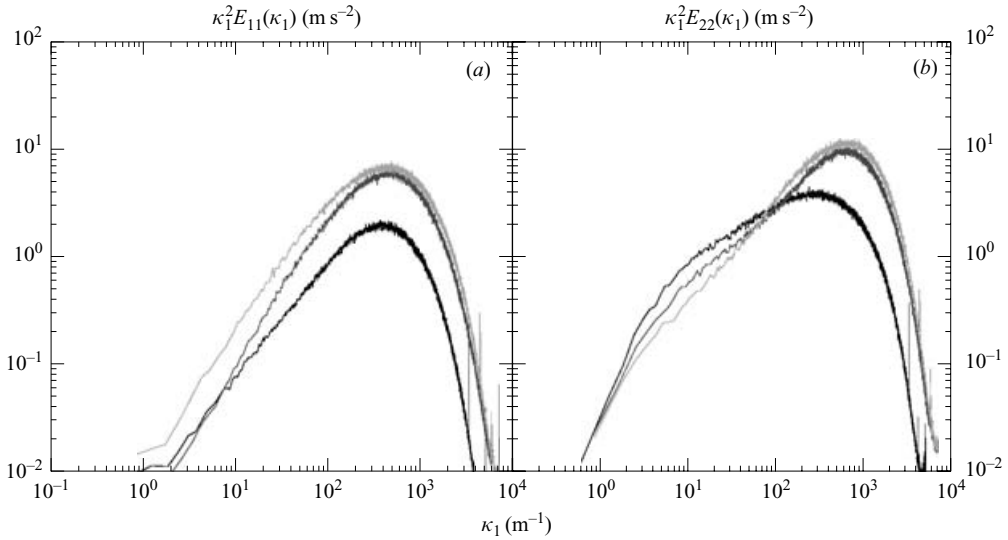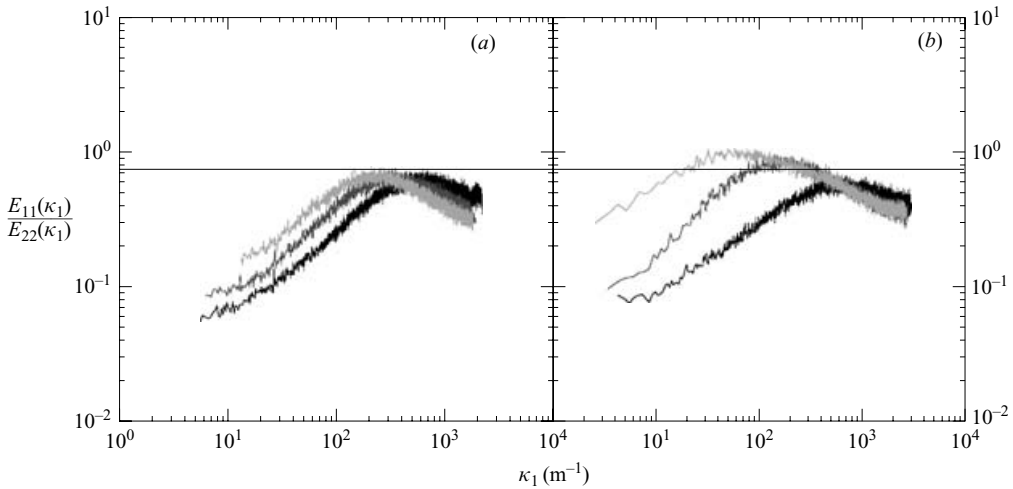
FIGURE 22. One-dimensional dissipation spectra, downstream evolution, active grid, long precontraction (RL), $R_{\lambda_a} = 260$, $\overline{S}^* = 24$: (a) $\kappa_1^2 E_{11}(\kappa_1)$; (b) $\kappa_1^2 E_{22}(\kappa_1)$; black line, station b; dark grey line, intermediate station; light grey line, station e.

FIGURE 23. Energy spectra ratio, downstream evolution. (a) 2.54 cm passive grid, short precontraction (1PS), $R_{\lambda_a} = 40$, $\overline{S}^* = 12$; (b) active grid, random mode, short pre-contraction (RS), $R_{\lambda_a} = 260$, $\overline{S}^* = 24$. Black line, station b; dark grey line, intermediate station; light grey line, station e. The horizontal line is the ratio in the inertial subrange for isotropic turbulence.

wavenumbers less than the peak wavenumber. This appears to be associated with the broadening of the transverse spectrum itself. These figures (21 and 22) also show that as the flow evolves the peaks of the longitudinal and transverse dissipation spectra become nearly equal, indicating that the flow is approaching small-scale isotropy (see also figures 23a and 23b).

The ratios of the evolving longitudinal and transverse spectra in the postcontraction region are shown in figure 23. Here the return to isotropy, beginning with the small
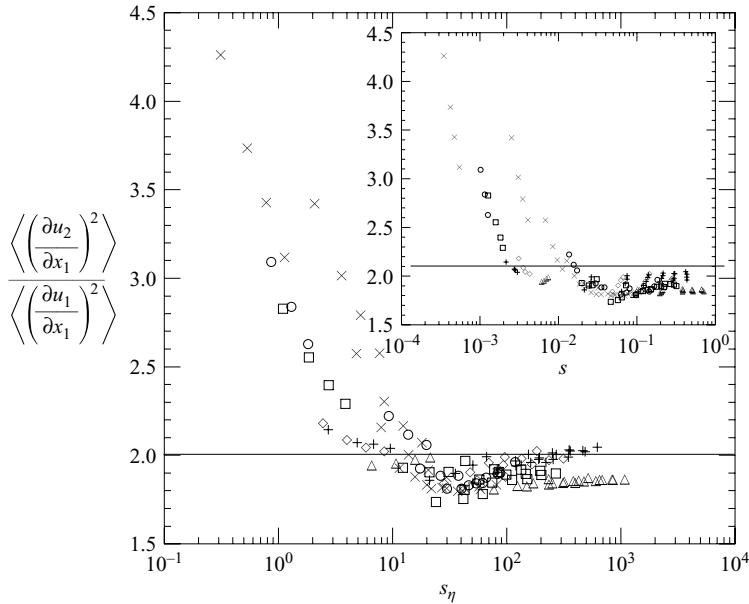
FIGURE 24. Postcontraction evolution of small-scale anisotropy as a function of s_η. s_η is the time normalized with the dissipation time scale (see text). Inset: post-contraction evolution of small-scale anisotropy with s (the normalized time). See figure 4 for meaning of the symbols.

scales, is nicely exhibited by the dilation of the region with negative slope as the flow evolves. As discussed above (figure 15), the ratio of these spectra decreases with wavenumber in isotropic turbulence.

In figure 8 we showed that in the immediate postcontraction region the small scales were isotropic for all but the very lowest Reynolds numbers. In figure 24 and its inset we plot the postcontraction ratio of the transverse and longitudinal derivative velocity variances, both as a function of s (see the discussion of figure 16) and of a new variable s_η, defined by

$$s_\eta \equiv \int_{x_b}^{x} \frac{1}{\tau_\eta} \frac{\mathrm{d}x}{\langle U_{1_b} \rangle} \tag{4.4}$$

where $\tau_\eta = (\nu/\langle \varepsilon \rangle)^{1/2}$ is the Kolmogorov time scale. Here the non-dimensional time is based on the dissipation rather than the integral scale. Both plots in figure 24 reflect the rapid return to isotropy of the small scales (note the logarithmic abscissa) even for the low-Reynolds-number turbulence. The dependence on s_η provides a slightly better collapse than the dependence on s.

The evolution of the longitudinal derivative skewness $S_{\partial u_1 / \partial x_1}$ (defined as $\langle (\partial u_1/\partial x_1)^3 \rangle / \langle (\partial u_1/\partial x_1)^2 \rangle^{3/2}$) is shown in figure 25. (The transverse derivative skewness is zero by symmetry and this was verified.) In isotropic turbulence the longitudinal derivative skewness has a value of approximately -0.4 and exhibits a slow variation with Reynolds number (VanAtta & Antonia 1980; Sreenivasan & Antonia 1997; Gylfason, Ayyalasomayajula & Warhaft 2004). The precontraction value we observe for the longitudinal derivative skewness is also close to -0.4 but the contraction causes a rapid increase in its value and, as the flow emerges from the contraction, the value becomes positive. Then as the flow returns towards isotropy in the straight section of the tunnel, the skewness returns to its initial value of -0.4. The same
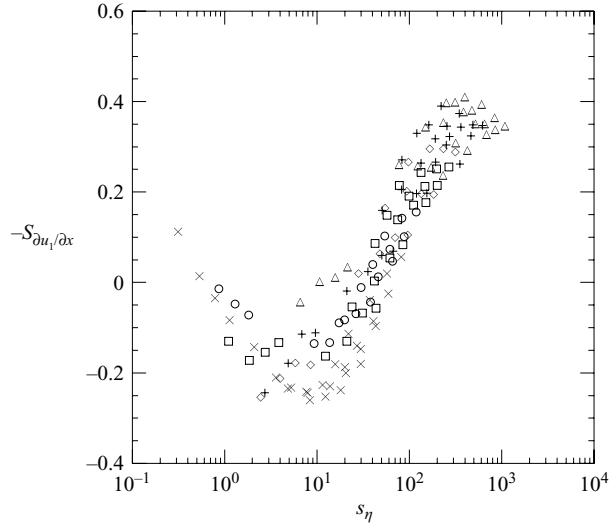
FIGURE 25. Post-contraction evolution of the skewness of $\partial u_1/\partial x$ as a function of s_η. The symbols have the same meaning as in figure 4.

effect was observed by Mills & Corrsin (1959) and more recently by Sjogren & Johansson (1998). Negative skewness in turbulence, be it isotropic grid turbulence or typical shear flows (jets, boundary layers etc.) is a manifestation of vortex stretching, which allows for a cascade from the large to the small scales. Without the negative skewness the cascade is inhibited. Clearly the dramatic change in the skewness implies a change in turbulence structure. In an equilibrium flow the positive sign might signify that vortex compression is dominating over stretching and that the flow consists of predominantly tube-like structures rather than sheets (Townsend 1951; Betchov 1956; Davidson 2004). It is not unreasonable to conjecture that the contraction causes the vortex sheets to evolve into tubes and that as the strain is released the intercomponent energy transfer allows for a relaxation back to the equilibrium state. Notice that there is some overshoot: after the flow emerges from the contraction the skewness keeps increasing for a short distance in the straight section, and this may be related to the persistence of a mean strain in the postcontraction region (figure 2). Note also the relatively good collapse of the various experiments at different Reynolds numbers and different strain rates.

A typical set of normalized skewness spectra (multiplied by wavenumber to provide information on the peak 'energy') for a low-Reynolds-number low-strain case is shown in figure 26. The full spectrum becomes positive after the contraction and, as the flow evolves, the lower wavenumbers become negative first, indicating that the larger scales are restored before the smaller scales (relatively speaking; note that all the 'energy' of this derivative quantity resides at the higher wavenumbers). The skewness spectra at higher Reynolds numbers behave in a qualitatively similar way.

Finally, figure 27 shows the evolution of the derivative kurtosis for the u_1 and u_2 fluctuating components ($K_{\partial u_1/\partial x_1} \equiv \langle(\partial u_1/\partial x_1)^4\rangle/\langle(\partial u_1/\partial x_1)^2\rangle^2$ and $K_{\partial u_2/\partial x_1} \equiv \langle(\partial u_2/\partial x_1)^4\rangle/\langle(\partial u_2/\partial x_1)^2\rangle^2$). There appears to be a bifurcation: the higher-Reynolds-number active-grid results show high kurtosis after exiting the contraction and then rapidly decline, while the lower-Reynolds-number results exhibit a lag, peaking at an s_η value of around 10. We think that the difference is due to the lack of data at small s_η for the high-Reynolds-number case (note the logarithmic abscissa). For these
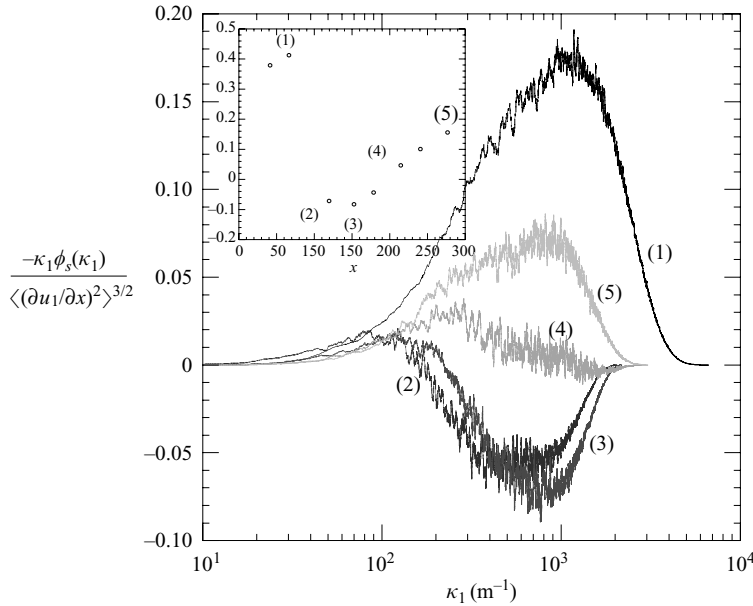
FIGURE 26. Skewness spectra $-\kappa_1\phi_s(\kappa_1)/\langle(\partial u_1/\partial x)^2\rangle^{3/2}$, downstream evolution, 2.54 cm passive grid, short precontraction (1PS), $R_{\lambda_1} = 44$, $\overline{S}^* = 12$. (Inset shows the derivative skewness, $-S_{\partial u_1/\partial x}$ vs x.) (1) station a; (2) station b; (3) and (4) intermediate stations; (5) station e.
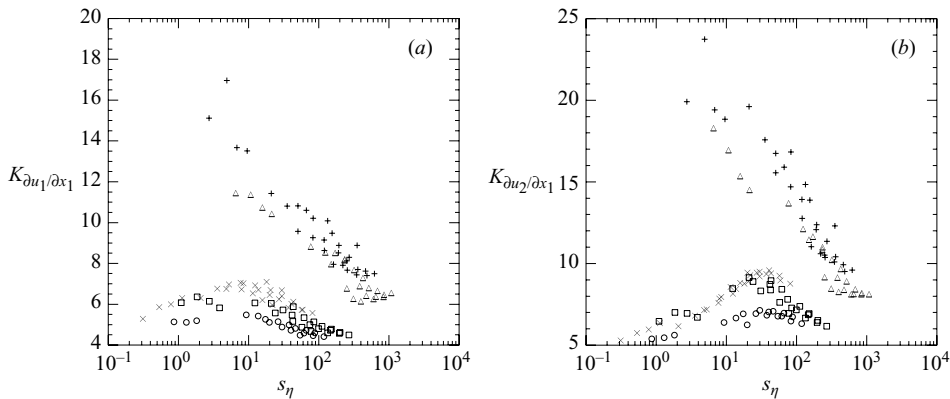

FIGURE 27. Evolution of the kurtosis of (a) $\partial u_1/\partial x_1$ and (b) $\partial u_2/\partial x_1$. The symbols have the same meaning as in figure 4.

data we could not get close enough to the exit of the contraction to resolve small s_η values. We suspect that the high-Reynolds-number data would exhibit a rise for small s_η. Notice that the u_1 and u_2 derivative kurtosis measurements are qualitatively similar, but the magnitudes of the transverse component are greater (as is observed in isotropic turbulence and in shear flows; see e.g. Sreenivasan & Antonia 1997).

The derivative kurtosis is an indicator of internal intermittency, and the postcontraction results suggest that the flow does become more intermittent. The reason for internal intermittency is far from resolved, but traditional theories assume that it is due to small-scale structures (e.g. Sreenivasan & Antonia 1997). For

the postcontraction region, we believe that the amplification may be due to a rearrangement of vortex structures by the mean strain.

5. Conclusions

The most significant finding of this experiment is that irrotational axisymmetric strain, acting over a broad range of scales, gives rise to nonlinear interactions. Thus we have observed that the strain shifts the peak of the longitudinal, u_1, spectrum to high wavenumbers relative to that of the transverse, u_2, spectrum (figures 10, 11 and 12). As the flow relaxes, after the strain has been removed, there is a multiscale interaction between the various spectral components, with the result that at high Reynolds number there is a complex double-peaked transverse spectrum, the high-wavenumber peak corresponding to the peak in the longitudinal spectrum (figures 19 and 20). Although most pronounced at the higher Reynolds numbers, there is evidence of non-local effects even at low Reynolds number (figures 18 and 20). In hindsight, these nonlinear effects are evident in the spectra of the low-Reynolds-number experiments of Warhaft (1980). Yet because the Reynolds number was not varied, these effects went unnoticed.

The measurements presented here are single-point, and we were unable to probe the details of the multiscale long-range interactions between the various spectral modes. However, by varying the initial conditions, we were able to determine that our results depend neither on the anisotropy level of the prestrained turbulence nor on the way the turbulence was generated. Thus, the precontraction anisotropy (based on velocity r.m.s. ratios) was varied from 1 to 1.7 (figure 7c) without any significant variation in the nature of the strained velocity field, and various passive and active grids were employed, but here too the results were qualitatively similar, independent of the grid type (figures 7 and 20). It might be argued that the nonlinearities are due to anisotropy in the precontraction vorticity structure (not measured), yet other experimental evidence (Antonia, Zhou & Zhu 1998) indicates that (passive) grid turbulence produces a close-to-isotropic vorticity field. The qualitative similarity between the active and passive grid results presented here suggests that the active grid precontraction velocity structure is not vastly different from that of passive grids (apart from being at higher Reynolds number). Further, we are inclined not to attribute our results to the non-uniformity of the strain itself. We have shown (figures 2 and 5) that although the strain rate varies within the contraction this variation is relatively small. Thus, we believe that the complex postcontraction velocity structure is due to the straining action as a function of wavenumber and is not strongly dependent on the initial conditions or on the variation in strain within the contraction. Nevertheless these issues require further study.

The strain causes a change in the sign of the velocity derivative skewness (figures 25 and 26) and increases the postcontraction velocity derivative kurtosis (figure 27). These effects are thought to be due to the change in the turbulence structure (possibly from sheets to tubes) by the straining motion and to the alignment of the structures by the strain. As the flow evolves in the postcontraction region, the flow relaxes back to 'normal' turbulence statistics, with a negative derivative skewness (~ -0.4) and a reduced derivative kurtosis. Constrained by our apparatus, our experiments were done for moderate strain rates ($10 \leqslant S^* \leqslant 35$, figure 4). Yet this appears to be the most interesting range to study since it spans the wavenumber variation from rapid straining of the large eddies to very weak strain effects on the small eddies (figures 15

and 23). For the limits of very large or very small $\overline{S}^*$ the nonlinear effects observed here probably would not occur.

Our experiments produce results that are at variance with classical RDT. This is to be expected since the straining is not homogeneous and the distortion is not rapid. Despite this we find reasonable agreement between simple RDT and integrated quantities (figure 7). Using asymptotic analysis, Kevlahan & Hunt (1997) made the point that RDT may be accurate for $S^* \sim 1$ because the straining motion modifies the turbulence in such a way that the nonlinear terms are inhibited. This was based mainly on their computation of integrated quantities such as the turbulence energy. Our results suggest that nonlinear effects are very important in determining the spectral dynamics of the velocity field. Further light on non-homogeneous flows such as those in the present study may be shed by the implementation of non-homogeneous RDT (Nazarenko, Kevlahan & Dubrulle 1999, 2000).

Our results also provide insight into why simple models are unable to describe the return-to-isotropy process accurately (figures 16 and 17). We have shown that a comparatively simple irrotational axisymmetric strained flow produces a very complex flow field and that proper modelling will require spectral rather than single-point closures.

REFERENCES

ANTONIA, R. A., ZHOU, T. & ZHU, Y. 1998 Three-component vorticity measurements in a turbulent grid flow. *J. Fluid Mech.* **374**, 29–57.

BATCHELOR, G. K. 1953 *The Theory of Homogenous Turbulence*. Cambridge University Press.

BATCHELOR, G. K. & PROUDMAN, I. 1954 The effect of rapid distortion of a fluid in turbulent motion. *Q. J. Mech. App. Maths* **7**, 83–103.

BELCHER, S. E. & HUNT, J. C. R. 1998 Turbulent flow over hills and waves. *Annu. Rev. Fluid Mech.* **30**, 507–538.

BETCHOV, R. 1956 An inequality concerning the production of vorticity in isotropic turbulence. *J. Fluid Mech.* **1**, 497–504.

CHOI, K. S. & LUMLEY, J. L. 2001 The return to isotropy of homogeneous turbulence. *J. Fluid Mech.* **436**, 59–84.

CHUNG, M. K. & KIM, S. K. 1995 A nonlinear return-to-isotropy model with reynolds-number and anisotropy dependency. *Phys. Fluids* **6**, 1425–1437.

DAVIDSON, P. A. 2004 *Turbulence: An Introduction for Scientists and Engineers*. Oxford University Press.

GENCE, J. N. & MATHIEU, J. 1980 The return to isotropy of an homogeneous turbulence having been subjected to successive plain strains. *J. Fluid Mech.* **101**, 555–566.

GOLDSTEIN, M. E. & DURBIN, P. A. 1980 The effect of finite turbulence spatial scales on the amplification of turbulence by a contracting stream. *J. Fluid Mech.* **98**, 473–508.

GOLDSTEIN, S. 1951 *Modern Developments in Fluid Dynamics*, vol. 1. Dover.

GYLFASON, A., AYYALASOMAYAJULA, S. & WARHAFT, Z. 2004 Intermittency, pressure and acceleration statistics from hot-wire measurements in wind-tunnel turbulence. *J. Fluid Mech.* **501**, 213–229.

HUNT, J. C. R. 1973 A theory of turbulent flow round two dimensional bluff bodies. *J. Fluid Mech.* **61**, 625–706.

HUNT, J. C. R. & CARRUTHERS, D. J. 1990 Rapid distortion theory and the problems of turbulence. *J. Fluid Mech.* **212**, 497–532.

Hunt, J. C. R., Kawai, H., Ramsey, S. R., Penrizetti, G. & Perkins, R. J. 1990 A review of velocity and pressure fluctuations in turbulent flows around bluff bodies. *J. Wind Engng Ind. Aero.* **35**, 49–85.

Hunt, J. C. R. & Snyder, W. H. 1980 Experiments on stably and neutrally stratified flow over a model two-dimensional hill. *J. Fluid Mech.* **96**, 671–704.

Kassinos, S. C., Reynolds, W. C. & Rogers, M. M. 2001 One-point turbulence structure tensors. *J. Fluid Mech.* **428**, 213–248.

Kevlahan, N. K. R & Hunt, J. C. R. 1997 Nonlinear interactions in turbulence with strong irrotational straining. *J. Fluid Mech.* **337**, 333–364.

Kida, S. & Hunt, J. C. R. 1989 Interaction between different scales of turbulence over short times. *J. Fluid Mech.* **201**, 411–445.

Launder, B. E., Reece, G. J. & Rodi, W. 1975 Progress in development of a reynolds-stress turbulence closure. *J. Fluid Mech.* **68**, 537–566.

Lee, M. J. 1986 Numerical experiments on the structure of homogeneous turbulence (distortion, relaxation, anisotropy, Navier-Stokes) PhD thesis, Stanford University.

Lee, M. J. 1989 Distortion of homogeneous turbulence by axisymmetric strain and dilatation. *Phys. Fluids.* **9**, 1541–1557.

Lee, M. J., Piomelli, U. & Reynolds, W. C. 1986 Useful formulas in the rapid distortion theory of homogeneous turbulence. *Phys. Fluids* **29**, 3471–3474.

Lee, M. J. & Reynolds, W. C. 1985 On the structure of homogeneous turbulence. *NASA Tech. Mem.* 19860045532.

Lumley, J. L. & Newman, G. R. 1977 Return to isotropy of homogeneous turbulence. *J. Fluid Mech.* **82**, 161–178.

Makita, H. 1991 Realization of a large-scale turbulence field in a small wind tunnel. *Fluid Dyn. Res.* **8**, 53–64.

Mills, R. R. & Corrsin, S. 1959 Effect of contraction on turbulence and temperature fluctuations generated by a warm grid. *NASA Tech. Mem.* 19980228031.

Mydlarski, L. & Warhaft, Z. 1996 On the onset of high reynolds number grid-generated wind–tunnel turbulence. *J. Fluid Mech.* **320**, 331–368.

Mydlarski, L. & Warhaft, Z. 1998 Passive scalar statistics in high-peclet-number grid turbulence. *J. Fluid Mech.* **358**, 135–175.

Nazarenko, S., Kevlahan, N. K.-R. & Dubrulle, B. 1999 WKB theory for rapid distortion of inhomogeneous turbulence. *J. Fluid Mech.* **390**, 325–348.

Nazarenko, S., Kevlahan, N. K.-R. & Dubrulle, B. 2000 Nonlinear rdt theory of near-wall turbulence. *Physica* D **139**, 158–176.

Newman, G. R., Launder, B. E. & Lumley, J. L. 1981 Modeling the behaviour of homogeneous scalar turbulence. *J. Fluid Mech.* **111**, 217–232.

Pearson, J. R. A. 1959 The effect of uniform distortion on weak homogeneous turbulence. *J. Fluid Mech.* **5**, 274–288.

Pope, S. B. 2000 *Turbulent Flows*. Cambridge University Press.

Prandtl, L. 1933 Attaining a steady air stream in wind tunnels. *NACA Tech. Mem.* 726.

Reynolds, A. J. & Tucker, H. J. 1975 Distortion of turbulence by general uniform irrotational strain. *J. Fluid Mech.* **68**, 673–693.

Reynolds, W. C. & Kassinos, S. C. 1995 One-point modelling of rapidly deformed homogeneous turbulence. *Proc. R. Soc. Lond.* A **451**, 87–104.

Ribner, H. S. & Tucker, M. 1953 Spectrum of turbulence in a contracting stream. *NACA Tech. Rep.* 1113.

Rotta, J. 1951 Statistische Theorie Nichthomogener Turbulenz 1. *Z. Phys.* **129**, 547–572.

Savill, A. M. 1987 Recent developments in rapid-distortion theory. *Annu. Rev. Fluid Mech.* **19**, 531–575.

Sirivat, A. & Warhaft, Z. 1983 The effect of a passive cross-stream temperature gradient on the evolution of temperature variance and heat flux in grid turbulence. *J. Fluid Mech.* **128**, 323–346.

Sjogren, T. & Johansson, A. V. 1998 Measurement and modelling of homogeneous axisymmetric turbulence. *J. Fluid Mech.* **374**, 59–90.

Sreenivasan, K. R. & Antonia, R. A. 1997 Phenomenology of small-scale turbulence. *Annu. Rev. Fluid Mech.* **29**, 435–472.

TAYLOR, G. I. 1933 Turbulence in a contracting stream. *Zeit. Angew. Math. Mech.* **15**, 91–96.

TOWNSEND, A. A. 1951 On the fine–scale structure of turbulence. *Proc. Roy. Soc. Lond.* A **208**, 534–542.

TOWNSEND, A. A. 1954 The uniform distortion of homogeneous turbulence. *Q. J. Mech. Appl. Maths.* **7**, 104–127.

TSINOBER, A. 2001 *An Informal Introduction to Turbulence*. Kluwer.

TUCKER, H. J. & REYNOLDS, A. J. 1968 Distortion of turbulence by irrotational plain strain. *J. Fluid Mech.* **32**, 657–673.

UBEROI, M. S. 1956 Effect of wind-tunnel contraction on free-stream turbulence. *J. Aero. Sci.* **23**, 754–764.

VANATTA, C. W. & ANTONIA, R. A. 1980 Reynolds number dependence of skewness and flatness factors of turbulent velocity derivatives. *Phys. Fluids.* **23**, 252–257.

WARHAFT, Z. 1980 An experimental study of the effect of uniform strain on thermal fluctuations in grid-generated turbulence. *J. Fluid Mech.* **99**, 545–573.